Title ： Dual targeting of astrocytic and endothelial GLUT1 enables functional rescue in GLUT1 deficiency syndrome

Shoko Tamura[1], Hiroko Shimbo[1], Nobuyuki Aruga[1,2], Haruo Okado[1], Yuga Yasuda[3], Yuichiro Miyaoka[3], Ayano Sasakura[4,5], Kinya Matsuo[4,6], Hideaki Nishihara[4,7], Erika Seki[8], Kazunari Sekiyama[8], Kenichi Oshima[8], Shinobu Hirai[1]*

1. Brain Metabolic Regulation Group, Department of Basic Medical Sciences, Tokyo Metropolitan Institute of Medical Science, Tokyo, Japan
2. Graduate School of Medical and Dental Sciences, Science Tokyo, Tokyo, Japan
3. Regenerative Medicine Project, Tokyo Metropolitan Institute of Medical Science, Tokyo, Japan
4. Department of Neurology and Clinical Neuroscience, Yamaguchi University Graduate School of Medicine, Yamaguchi, Japan
5. Yamaguchi University Graduate School of Medicine, Yamaguchi, Japan
6. Department of Neurology, Yamaguchi Prefectural Grand Medical Center, Yamaguchi, Japan
7. Research Institute for Cell Design Medical Science, Yamaguchi University, Yamaguchi, Japan
8. Laboratory of Molecular Pathology and Histology, Center for Medical Research Cooperation, Tokyo Metropolitan Institute of Medical Science, Tokyo, Japan
9. Department of Psychiatry, Tokyo Metropolitan Matsuzawa Hospital, Tokyo, Japan

*Corresponding author: Shinobu Hirai

Brain Metabolic Regulation Group, Department of Psychiatry and Behavioral Sciences, Tokyo Metropolitan Institute of Medical Science, Tokyo, Japan
E-mail: hirai-sn@igakuken.or.jp
Tel: +81-03-5316-3100

Competing interests: The authors declare no competing interests.

Abstract

Glucose transporter 1 deficiency syndrome (GLUT1-DS) is a metabolic encephalopathy caused by impaired glucose transport into the brain. Although GLUT1 in brain microvascular endothelial cells at the blood-brain barrier has been recognized as essential for glucose transport into the brain, the role of astrocytic GLUT1 has remained uncertain, limiting progress in gene therapy for GLUT1-DS. Here we show that astrocytic GLUT1 is broadly expressed in both mouse and human brains and is indispensable for maintaining cerebrospinal fluid glucose, cognitive performance, and motor coordination. Conditional haploinsufficiency in either astrocytes or endothelial cells reproduced GLUT1-DS-like phenotypes, and full rescue required AAV-mediated GLUT1 restoration in both cell types. To this end, we developed AAV-AST, a blood-brain barrier-penetrant vector with strong astrocyte tropism, and identified a candidate regulatory element (Region d) that supports endogenous-like GLUT1 expression. Together, these findings establish dual targeting of astrocytic and endothelial GLUT1 as a rational therapeutic strategy and identify a regulatory-capsid framework for next-generation therapies for GLUT1-DS and related neuro-metabolic disorders.

Introduction

The human brain, though comprising only ~2% of body mass, accounts for nearly 20% of systemic glucose utilization[1,2]. Glucose uptake in the brain is primarily mediated by facilitative glucose transporters (GLUTs), of which 14 isoforms exist in humans[3]. Among these, glucose transporter 1 (GLUT1) is the dominant isoform at the blood–brain barrier, expressed abundantly in vascular endothelial cells[4,5].

Reduced expression or function of GLUT1 causes GLUT1 deficiency syndrome (GLUT1-DS), a rare metabolic encephalopathy first described in 1991[6]. Heterozygous *SLC2A1* mutations underlie most cases[7], with an incidence estimated at 1 in 24,300-60,600 births[8,9]. Patients present with a broad spectrum of symptoms, including seizures, abnormal eye-head movements, cognitive and motor delay, and impaired head growth[10]. This clinical heterogeneity complicates diagnosis for GLUT1-DS, and the true prevalence is likely underestimated. A reduced cerebrospinal fluid (CSF)-to-blood glucose ratio is the key diagnostic hallmark, seen in nearly all patients[11,12].

Current therapy relies on ketogenic diets, but their efficacy for seizures and cognitive and motor dysfunction is only partial[10,13,14]. Safety concerns remain, particularly during pregnancy[15]. These limitations underscore the urgent need for curative approaches. Gene therapy using adeno-associated virus (AAV) vectors has emerged as a promising strategy, with proof-of-concept studies demonstrating benefit in animal models[16-19]. Endothelial cells (ECs) have been considered the primary therapeutic target. This is based on the fact that GLUT1 expression has been classically regarded as selective to the capillary endothelium[5,20],

and that Glut1 deletion restricted to endothelial cells phenocopies systemic haploinsufficiency[17,21].

Nevertheless, evidence suggests that GLUT1 expression is not confined to ECs. Spatial transcriptomic datasets report Glut1 mRNA expression in microglia, oligodendrocytes, astrocytes, and neurons, although the corresponding protein distribution remains unclear (https://www.proteinatlas.org/). Several studies described astrocytic GLUT1 protein [22-24], but these findings were inconsistent and difficult to interpret given the limited resolution of early staining approaches. Astrocytes are thought to support neural activity through metabolic coupling, in which intracellularly imported glucose is converted to lactate and supplied to neurons via the astrocyte-neuron lactate shuttle [2,25,26]. Accordingly, the prevailing model has been that astrocytic GLUT1 is concentrated at perivascular endfeet, where it mediates uptake of blood-derived glucose for lactate production.

Here we show, using a mouse model, that astrocytic GLUT1 is required for glucose entry into the brain parenchyma and for maintaining brain glucose homeostasis, suggesting that effective therapy for GLUT1-DS may require restoring GLUT1 in both endothelial and astrocytic compartments. However, astrocytes remain difficult to transduce, as conventional AAV serotypes preferentially target neurons or endothelium while transducing astrocytes inefficiently[27,28]. In parallel, precise transcriptional regulatory elements are needed to restrict therapeutic GLUT1 expression to relevant cell types. We therefore delineate the roles of endothelial and astrocytic GLUT1 and develop an astrocyte-tropic AAV platform and regulatory element to enable rational dual targeting and functional rescue.

Results

GLUT1 is expressed in both endothelial cells and astrocytes in mouse and human brains

We first assessed the cellular distribution of Glut1 (GLUT1) in the mouse and human brain. In mice, Glut1 was abundantly expressed across the brain parenchyma (Fig. 1A). While conventional immunohistochemistry primarily localized Glut1 to vascular ECs, enhanced detection with the avidin-biotin complex (ABC) method revealed extensive expression in astrocytes as well. Notably, the labeling extended continuously from perivascular endfeet along the soma to distal astrocytic processes (Fig. 1B). Similarly, in the human postmortem brains, GLUT1 was strongly expressed in ECs and weakly but broadly in astrocytes (Fig. 1C). These findings indicate that astrocytic GLUT1 expression is not confined to perivascular regions but is distributed throughout the entire astrocytic soma and processes.

Both astrocytic and endothelial GLUT1 deficiency contribute to cognitive and motor impairments

To determine the functional relevance of astrocytic GLUT1, we compared systemic Glut1 heterozygous mice (Glut1 del/+) with conditional heterozygotes lacking one allele in astrocytes (Aldh1l1-Cre; Glut1 flox/+) or ECs (Tie2-Cre; Glut1 flox/+) (Fig. 2). Systemic Glut1 del/+ mice have been reported to show cognitive impairments resembling those in GLUT1 deficiency syndrome (GLUT1-DS) patients[21]. In both the object location test (OLT) and novel object recognition test (NORT), astrocyte-specific and EC-specific heterozygotes displayed significantly lower discrimination index scores than wild-type (WT) controls (OLT: $p < 0.0001$ and $p = 0.0002$; NORT: $p = 0.0012$ for both), closely paralleling deficits in Glut1 del/+ mice (Fig. 2A, B).

Motor coordination, one of the hallmark deficits in GLUT1-DS, was then evaluated using the slip test. As previously reported, EC-specific Glut1 deficiency impairs rotarod performance[17], Consistent with this, EC-specific heterozygotes showed significant deficits compared with WT controls, and notably, astrocyte-specific heterozygotes exhibited comparable impairments ($p < 0.0001$, $p = 0.0006$, and $p = 0.0180$, respectively) (Fig. 2C). Together, these results indicate that both astrocytic and endothelial GLUT1 are indispensable for maintaining normal cognitive and motor functions.

Glut1 deficiency in astrocytes and ECs lowers CSF-to-blood glucose ratio without altering blood glucose

Because a reduced cerebrospinal fluid (CSF)-to-blood glucose ratio is a diagnostic hallmark of GLUT1-DS, we next assessed glucose concentrations (Fig. 2D). While blood glucose levels were unchanged across groups (Supplementary Fig. 1), CSF-to-blood glucose ratio was significantly reduced in Glut1 del/+, Aldh1l1-Cre; Glut1 flox/+, and Tie2-Cre; Glut1 flox/+ mice compared to WT controls ($p < 0.0001$ for each). These results confirm that GLUT1 in both astrocytes and ECs is necessary for sustaining CSF glucose homeostasis.

Both astrocytic and endothelial GLUT1 are required for brain glucose uptake

To directly evaluate brain glucose uptake, we monitored thalamic interstitial fluid (ISF) glucose concentrations after oral glucose administration (0.03 g per mouse) (Fig. 2E,F). Thalamic glucose uptake, as identified by [^18F]-FDG positron emission tomography, is known to be reduced in GLUT1-DS patients[29]. ISF glucose elevation was markedly attenuated in systemic, astrocyte-specific, and EC-specific Glut1 heterozygotes compared with WT controls ($p < 0.0001$ for each). These findings establish that astrocytic and endothelial GLUT1 jointly enable glucose entry into the brain parenchyma in response to systemic glucose fluctuations.

Development of AAV-AST: a BBB-penetrant vector with robust astrocyte tropism

To develop an astrocyte-targeted gene therapy approach, we rationally engineered an AAV-based capsid containing an optimized heptapeptide insertion within the VR-VIII loop. We reanalyzed previously published AAV insertion library datasets to identify reference motifs

associated with astrocyte/CNS tropism.[30-33] Position-specific analysis of normalized 7-mer insertions identified a T(L/A/T)xxPF[K/L] core architecture characterized by enrichment of Thr at position 1 and Pro-Phe at positions 5–6. This positional pattern was also evident in the sequence logo generated from the position-frequency matrix (Supplementary Fig. 2A). Because several literature-supported astrocyte/CNS-related motifs mapped onto closely related PHP.B-like branches, candidate prioritization was performed using a branch-aware motif compatibility score rather than a single pooled logo score. Using this framework, TLAVPFK, TLQLPFK, TTLKPFL, and TALKPFL ranked within the top-scoring group (Supplementary Fig. 2B). Because TLAVPFK is identical to the PHP.eB insertion sequence, it was excluded from experimental testing, and the next three top-ranked motifs were selected for in vivo validation. These were designated AAV-AST0 (TTLKPFL), AAV-AST1 (TALKPFL), and AAV-AST3 (TLQLPFK). All three retain the conserved T(L/A/T)xxPF[K/L] core architecture while introducing branch-specific sequence divergence.

To functionally validate these candidates, we performed intravenous administration in mice. AAV-AST0 failed to traverse the murine BBB and showed only limited CNS transduction (Supplementary Fig. 2C). In contrast, AAV-AST3 crossed the BBB and robustly transduced astrocytes, but it also transduced neurons at a similar magnitude, prompting us to exclude it from further analyses. (Supplementary Fig. 2D). Among the variants tested, AAV-AST1 displayed the most favorable profile, combining efficient BBB penetration with pronounced astrocyte selectivity. This screening yielded a variant capable of crossing the BBB, which we designated AAV-AST. We selected AAV-AST1 (TALKPFL insertion) as the lead candidate and hereafter refer to it as AAV-AST.

Following intravenous delivery, AAV-AST mediated widespread and efficient gene transfer throughout the brain, with a strong preference for astrocytes and minimal transduction of neurons and other CNS cell types (Fig. 3A). Astrocyte tropism was particularly pronounced in juvenile mice (Fig. 3B, C). We next evaluated transduction in primary human astrocytes. Compared with the control capsids AAV9 and PHP.eB, AAV-AST achieved significantly higher transduction efficiency (Fig. 3D-F). In mice, PHP.eB has been shown to cross the blood–brain barrier efficiently and mediate broad CNS transduction, including astrocytes[34]. AAV9 is an AAV serotype currently used for intravenous gene therapy in human neurological diseases[35]. Together, these results suggest that AAV-AST represents a clinically relevant platform for astrocyte-directed gene delivery.

Targeting both astrocytes and ECs is necessary for effective GLUT1 gene therapy

To determine the extent to which dual targeting is required for phenotypic rescue, we performed intravenous rescue experiments in Glut1 del/+ mice using AAV vectors that preferentially transduce vascular endothelial cells (AAV-BR1[36] and AAV-X1.1[37]) and an astrocyte-tropic vector (AAV-AST). Vectors encoding GLUT1-myc-T2A-mCherry under the CAG promoter were administered by retro-orbital injection between postnatal days 15 and 19 (P15-19) (Supplementary Fig. 3), either to restore GLUT1 in a single cell type (endothelium or astrocytes) or simultaneously in both. In behavioral analyses, object

location memory (OLT) was significantly improved by either endothelial- or astrocyte-directed supplementation, whereas the dual-targeting regimen produced the most pronounced rescue relative to vehicle-treated heterozygotes (Fig. 4A). Similarly, the CSF-to-blood glucose ratio was partially restored by single-cell-type supplementation and further enhanced by dual targeting, approaching wild-type levels (Fig. 4E). In contrast, in the novel object recognition test (NORT), single-cell-type supplementation did not produce a detectable rescue, whereas dual supplementation restored performance, indicating that concurrent restoration in both compartments is required for this cognitive domain (Fig. 4B). Motor coordination deficits assessed by the foot-slip test were not significantly improved in any rescue group compared with Glut1 del/+ controls under this treatment paradigm (Fig. 4C). Random-fed blood glucose remained unchanged across all viral and control groups (Fig. 4D).

Identification of a regulatory region enabling endogenous GLUT1 expression

Having established that optimal phenotypic rescue requires restoring GLUT1 in both endothelial cells and astrocytes, we next asked whether therapeutic expression could be placed under endogenous-like transcriptional control. We therefore prioritized candidate cis-regulatory elements at the SLC2A1 (GLUT1) locus by integrating H3K27ac ChIP-seq tracks in the UCSC Genome Browser (https://genome.ucsc.edu/index.html), ENCODE-annotated candidate regions, and a previously reported SLC2A1 regulatory sequence, which was used as a reference sequence in subsequent analyses[38] (Fig. 5A). Nine candidate sequences (a-i) were cloned upstream of an mCherry reporter and co-transfected with a CAG-GFP plasmid as a transfection control (Fig. 5B-D and Supplementary Fig. 4). In both human brain microvascular endothelial cells (hBMECs) (Fig. 5B, C) and primary cultured human astrocytes (Fig. 5D and Supplementary Fig. 4), only Region d exhibited reporter activity significantly higher than Ref. when quantified after normalization to CAG-GFP. These results identify Region d as a candidate cis-regulatory element for driving SLC2A1-like expression and support its potential use in combination with endothelial- and astrocyte-tropic AAV vectors for dual-targeted GLUT1 supplementation.

Cross-context validation of Region d regulatory activity in vivo and in human iPSC-derived cells

To evaluate whether the regulatory activity of Region d identified in vitro is preserved in vivo, a reporter construct containing this regulatory element was packaged into an AAV-V1 capsid and systemically administered to mice by retro-orbital injection (Fig. 6A). To interrogate the function of the regulatory element using a single capsid, we chose AAV-V1, an AAV serotype capable of transducing both vascular endothelial cells and astrocytes in mice[31]. Region d drove reporter expression restricted to vascular endothelial cells and astrocytes, thereby recapitulating the endogenous SLC2A1 (GLUT1) expression pattern, although reporter expression remained modest.

To enhance expression strength without altering cell-type specificity, a CMV enhancer was placed upstream of Region d[39] (hereafter referred to as Region d□; Fig. 6B). This modification markedly increased the number of mCherry-positive cells in both vascular endothelial cells and astrocytes, resulting in a signal distribution and intensity more closely resembling endogenous GLUT1 expression.

Because direct validation in human tissues is not feasible, we next assessed the regulatory activity of these elements in human iPSC-derived cells using capsids selected for their distinct tropisms. Specifically, AST-Region Ref., AST-Region d and AST-Region d□, as well as X1.1-Region Ref., X1.1-Region d and X1.1-Region d□, were tested in human iPSC-derived astrocytes and endothelial cells, respectively (Fig. 6C-E). In these human cellular models, Region d□ consistently drove the most robust reporter expression, indicating that the enhancer-coupled configuration retains regulatory activity in a human context. Notably, these experiments also showed that both AAV-AST and AAV-X1.1 can efficiently transduce their respective human iPSC-derived target cells, supporting the relevance of these capsids beyond the mouse system.

Together, these findings support Region d as a functional cis-regulatory element capable of supporting endogenous-like GLUT1 expression across both mouse in vivo and human iPSC-derived settings, while identifying Region d□ as an optimized configuration with enhanced expression strength. Moreover, the successful transduction of human iPSC-derived astrocytes and endothelial cells by AAV-AST and AAV-X1.1, respectively, underscores the translational potential of this regulatory-capsid platform for gene delivery to both vascular endothelial cells and astrocytes. These results support a modular strategy for AAV-based therapeutic development, in which appropriate regulatory elements are combined with cell-targeting capsids, including AAV-AST and AAV-X1.1, to enable adaptation to a broad range of diseases.

Discussion

In this study, we provide direct evidence that GLUT1 is expressed not only in vascular endothelial cells (ECs) but also widely in astrocytes in human and mouse brains. This distribution extends well beyond perivascular endfeet, underscoring that astrocytes, long considered metabolic supporters, are themselves central to brain glucose homeostasis (Supplementary Fig. 5). Functionally, we demonstrate that reduction of Glut1 expression in either ECs or astrocytes alone was sufficient to induce phenotypes closely resembling GLUT1 deficiency syndrome (GLUT1-DS), including cognitive and motor impairments as well as reductions in cerebrospinal fluid (CSF)-to-blood glucose ratios. These findings establish that both astrocytic and endothelial GLUT1 are indispensable for maintaining brain metabolism and function.

Previous spatial transcriptomic datasets have shown that Glut1 mRNA is expressed in multiple non-endothelial cell types, in addition to endothelial cells (https://www.proteinatlas.org/), and protein-level detection primarily in ECs by using immunoblotting and immunohistochemistry[5,20]. Astrocytic GLUT1 has been thought to localize mainly at perivascular endfeet[5,22]. By integrating these fragmented observations, our study demonstrates widespread GLUT1 distribution throughout astrocytic membranes in both human and mouse brains (Fig. 1). Interestingly, in mice, all genetically labeled astrocytes expressed GLUT1, whereas in human brains, some astrocytes expressed GLUT1 while others did not, consistent with the evolutionary expansion of astrocytic diversity[40,41]. These results suggest that human astrocytes may exhibit more specialized metabolic subtypes than those in rodents.

Systemic Glut1 heterozygous mice recapitulate cardinal features of GLUT1-DS, including reduced CSF-to-blood glucose ratios and impaired neurodevelopment, motor coordination, and seizure susceptibility[42]. EC-specific Glut1 heterozygotes similarly display reduced CSF glucose and motor impairments[4,17]. Extending these findings, we show here that astrocyte-specific heterozygotes also develop cognitive and motor deficits with decreased CSF-to-blood glucose ratios, thereby highlighting that astrocytic Glut1 contributes as critically as endothelial Glut1 to GLUT1-DS pathogenesis (Fig. 2).

Mechanistically, astrocytes take up glucose through their perivascular endfeet and metabolize it into lactate, regulating extracellular lactate concentrations through monocarboxylate transporter 1 (MCT1) and contributing to the astrocyte–neuron lactate shuttle[1,2,25,26]. On the other hand, glucose itself is present in the extracellular space and has been measured via microdialysis[43,44]. Neurons take up not only lactate but also glucose, primarily via GLUT3, whereas GLUT4 can be translocated to neuronal membranes under certain activity-dependent conditions[45-47]. Our biosensor-based analysis demonstrated that oral glucose uptake into the brain parenchyma was significantly impaired in systemic, EC-specific, and astrocyte-specific Glut1 heterozygotes (Fig. 2). Together, these findings suggest that extracellular glucose is also regulated by astrocytes, consistent with the distribution of GLUT1 across astrocytic membranes. Because GLUT1 operates as a facilitated transporter, astrocytes may mediate bidirectional glucose transport, coupling intracellular and extracellular gradients[48]. Given the close exchange between CSF and interstitial fluid[49], reductions in CSF glucose likely reflect impaired parenchymal glucose supply.

From a therapeutic perspective, the ketogenic diet remains the standard of care for GLUT1-DS, but its efficacy for cognitive and motor impairments is limited[50]. Consequently, gene therapy approaches using AAV vectors have been pursued[16,18,38]. Our findings show that restoring GLUT1 in either astrocytes or ECs alone was insufficient for robust recovery, whereas dual targeting achieved substantial functional improvement, normalizing the CSF-to-blood glucose ratio and ameliorating cognitive deficits (Fig. 4). This underscores that successful gene therapy must simultaneously address both cell types.

Notably, motor coordination was not rescued under our treatment paradigm, consistent with previous work showing that later interventions fail to restore motor function[19]. This

aligns with evidence that motor phenotypes arise from early-life glucose insufficiency and that treatment efficacy is strongly dependent on the developmental stage at initiation[17,50,51]. Thus, earlier intervention may be necessary to fully rescue motor outcomes in GLUT1-DS, paralleling the high glucose demand of the developing human brain[52].

One of the major challenges in CNS gene therapy is the reproduction of endogenous expression patterns in target cell types following systemic delivery. Our study identifies Region d as a candidate regulatory element that supports endogenous-like GLUT1 expression in both ECs and astrocytes (Fig. 5, 6 and Supplementary Fig. 4), helping address this key limitation. This concept is further supported by cross-context validation in human iPSC-derived astrocytes and endothelial cells. To achieve such dual targeting, complementary vector systems are required. X1.1, developed by others, has been experimentally demonstrated to efficiently transduce human vascular endothelial cells[37], whereas our newly developed AAV-AST mediates robust and preferential transduction of astrocytes (Fig. 3 and Supplementary Fig. 2). In principle, combining X1.1 and AAV-AST with Region d or Region d' (CMV–Region d) could provide a modular route toward endogenous-like GLUT1 expression across both cell types, forming a versatile platform for dual-targeted supplementation. Collectively, these findings support astrocyte-directed gene delivery as a component of future therapeutic strategies for GLUT1-DS and potentially a broader spectrum of astrocyte-related diseases. By enabling rationally engineered dual-targeting strategies, our work provides a framework for the clinical translation of AAV-based therapies that harness astrocytes as active therapeutic targets.

Conclusion

In summary, we demonstrate that both astrocytic and endothelial GLUT1 are indispensable for maintaining brain glucose homeostasis and preventing the neurobehavioral phenotypes characteristic of GLUT1-DS. Our findings reveal that effective therapy requires dual targeting of these two cell types, and suggest that this goal may be pursued by combining Region d/Region d′ with AAV-AST and AAV-X1.1This dual-platform concept addresses key barriers in CNS gene therapy and highlights a path by which astrocytes may be harnessed as direct therapeutic targets. Beyond GLUT1-DS, this paradigm holds broad promise for a wide spectrum of astrocyte-related neurological disorders, offering a clear path from proof-of-concept toward clinical development.

Methods

Human postmortem brain tissue collection

Human postmortem brain tissues were obtained from the Tokyo Metropolitan Matsuzawa Hospital. The use of postmortem human brain tissues in the present study was approved by the Ethics Committee of Tokyo Metropolitan Institute of Medical Science (no. 23-26) and

complied with the Declaration of Helsinki and its later amendments. All procedures were conducted with the informed written consent of the next of kin.

Immunohistochemistry of Postmortem Brain Tissue

Tissue sections were permeabilized with PBS containing 0.3% Triton X-100 for 30 min at room temperature (R.T.), followed by quenching of endogenous peroxidase activity with 1% aqueous hydrogen peroxide for 20 min. Heat-induced antigen retrieval was performed in Tris-HCl buffer (pH 9.5) at 98°C for 1 hour. After blocking with 10% normal goat serum in PBS containing 0.3% Triton X-100 for 1 hour, sections were incubated overnight at 4°C with primary antibodies against GLUT1 (rabbit; 1:200, Frontier Institute Co.,Ltd., Af610) and GLT-1 (guinea pig; 1:200, Millipore, A1783).

Following three washes in PBS containing 0.3% Triton X-100, sections were incubated for 2 hours at RT with biotinylated goat anti-rabbit IgG (1:1000, Vector, BA-1000) to detect GLUT1. After another set of washes, signal amplification was performed using the VECTASTAIN Elite ABC Kit (PK-6100) for 30 min. Sections were then blocked with 5% normal donkey serum in PBS containing 0.3% Triton X-100 for 15 min, followed by TrueBlack® Lipofuscin Autofluorescence Quencher (5% in 70% ethanol, Cosmo Bio, Tokyo, Japan) treatment for 30 sec.

For fluorescence detection, GLUT1 signal was developed with TSA-Cy5 (1:500) for 10 min. Sections were then incubated with donkey anti–guinea pig IgG Cy3 (1:500, Merck Millipore, AP193C) to detect GLT-1, together with DAPI (1:100, Dojindo, D523) for 2 hours at R.T. After final washes, sections were mounted with fluorescence mounting medium.

Animals

All experimental procedures were approved by the Animal Experimentation Ethics Committee of the Tokyo Metropolitan Institute of Medical Science (No. 24-034, approved on 1 April 2024). Animal care was provided in accordance with the institutional animal experimentation guidelines. All mice were maintained under controlled temperature (23 ± 1 °C), humidity (50 ± 10%), and 12:12 h light/dark cycle (lights on at 8:00 a.m.) with free access to a standard laboratory diet and water. All efforts were made to minimize the number of animals used and their suffering. Glut1 heterozygous mutant (Glut1 del/+) mice, used as a model for Glut1 deficiency syndrome (Glut1-DS)[42], were generated by crossing CAG-Cre mice (a kind gift from Dr. Murakami[53]) with floxed Glut1 mice (The Jackson Laboratory, stock no. 031871). This cross results in Cre-mediated deletion of the floxed Glut1 gene in oocytes, leading to systemic Glut1 deficiency in the offspring. Mice harboring the Tie2-Cre (stock no. #004128), Aldh1l1-Cre (stock no. #023748), Aldh1l1-CreERT2 (stock no. #029655) drivers, tdTomato-floxed STOP reporter mice (tdTomato reporter mice) (stock no. 007914) and floxed Glut1 mice (stock no. #031871) were all obtained from the Jackson Laboratory, backcrossed over 10 generations to the C57BL/6J genetic strain background. Homozygous Glut1 flox/flox mice were mated with Tie2-Cre and Aldh1l1-Cre mice to generate Tie2-Cre; Glut1 flox/+ and Aldh1l1-Cre; Glut1 flox/+ conditional heterozygous mice, respectively. Male and female mice were used in all experiments.

CSF and blood glucose measurements

CSF was extracted from the cisterna magna using a protocol described by Pegg et al.[54]. Mice were anesthetized by intraperitoneal injection of pentobarbital (34.5-51.8 mg/kg), which was chosen to minimize increases in blood glucose levels, and secured in the prone position. The head was tilted forward at an angle of approximately 25 degrees. Using a sterilized scalpel, the skin was incised, and the muscle layers were carefully separated to provide access to the cisterna magna, located between the occipital bone and the first cervical vertebra. Cerebrospinal fluid (CSF) was collected from the cisterna magna using sterilized glass capillaries (1B150F-4, World Precision Instruments) connected to a winged needle and syringe assembly. Samples contaminated with blood were discarded. The glucose concentration in the collected CSF was measured using a blood glucose meter (Abbott Laboratories).

Simultaneously with the CSF collection, blood was sampled from the tail tip. While the mouse was secured in a stereotaxic frame, a small incision was made at the tip of the tail using a razor blade, and 2–3 μl of blood was collected. The blood glucose level was immediately measured using a blood glucose meter (Abbott Laboratories).

Measurement of glucose uptake into brain parenchyma.

Extracellular glucose levels were measured using a commercially available in vivo biosensor recording system (Pinnacle Technology) according to the manufacturer's instructions. A guide cannula was stereotaxically implanted to target the thalamus (AP −1.5 mm, ML −1.3 mm, DV −2.0 mm), and mice were allowed to recover for 1 week. Immediately before each recording, the glucose biosensor (standard mouse sensor) was calibrated using known glucose concentrations following the manufacturer's protocol, and then inserted into the guide cannula. Recordings were initiated after the signal stabilized; mice were additionally allowed to equilibrate for 1 h after sensor insertion to ensure a stable baseline. Glucose (0.03 g per mouse) was administered by oral gavage, and extracellular glucose was continuously recorded at 1 Hz. Signals were transmitted from the potentiostat to a computer and acquired using Sirenia Acquisition Software (Pinnacle Technology). Glucose elevation was quantified as the difference between the baseline level immediately before gavage and the peak level observed after gavage. The glucose response was quantified as the peak ΔISF glucose (peak value minus the mean baseline value immediately before gavage).

Behavioral tests

Prior to each behavioral test, mice were acclimated to the behavioral testing room for at least 30 minutes. The object location test (OLT) and novel object recognition test (NORT) were performed to assess memory function[55], while motor function was evaluated using the slip test[56].

Both the OLT and NORT consisted of three sessions: habituation, learning, and test. Mice were first placed in the center of the test apparatus (33 × 50 × 40 cm) and allowed to explore freely for 10 minutes, followed by a 1-2 hour return to their home cage. During the familiarization session, two identical objects (A and B) were placed in adjacent corners, 5

cm from the walls of the arena. Mice were reintroduced to the arena for 5 minutes, then returned to their home cage for 5 minutes. For the OLT test session, object B was moved to a diagonally opposite corner (designated B'), and mice were allowed to explore the arena for an additional 5 minutes. NORT was conducted immediately afterward. Mice were returned to the home cage for 5 minutes, and object A was replaced with a novel object (object C) in the same location. Mice were then placed back in the arena for another 5-minute test session.

Exploration times for objects A, B', and C were recorded to calculate the discrimination indices as follows:

- OLT = (B' − A) / (B' + A)
- NORT = (C − B') / (C + B')
- where A, B', and C represent the time spent exploring each object.

All behavioral tests were conducted under ambient lighting conditions of 10–15 lux. Mouse behavior was recorded using a ceiling-mounted charge-coupled device (CCD) camera positioned above the apparatus.

For the slip test, mice traversed a horizontal grid while being monitored with a side-mounted CCD camera. The number of times the hindlimb and forelimb falling through the grid was counted over 50 steps.

Immunofluorescence staining of mouse brain tissue

Following transcardial perfusion with phosphate-buffered saline (PBS) and 4% paraformaldehyde (PFA), whole brains were extracted, post-fixed overnight at 4°C, and cryoprotected in 20% sucrose at 4°C for one week. Serial coronal sections (50µm thick) were prepared using a cryostat (CM3050 S; Leica Microsystems). Antigen retrieval was performed by incubating the sections in HistoVT One solution (Nacalai Tesque) at 70°C for 30 minutes in a water bath. Sections were then permeabilized with a solution containing 0.2% Triton X-100, 1% Block Ace (DS Pharma Biomedical) in PBS for 30 minutes at room temperature. This was followed by overnight incubation with primary antibodies in PBS containing 0.4% Block Ace at room temperature. The immunostaining protocol continued with three washes in PBST (PBS with 0.05% Tween 20), followed by a 3-hour incubation with fluorophore-conjugated secondary antibodies diluted in PBS containing 0.4% Block Ace and 0.05% sodium azide. Nuclei were counterstained with 4,6-diamidino-2-phenylindole (DAPI; Nacalai Tesque). Sections were subsequently washed three times in PBST, mounted in Fluoromount (Diagnostic BioSystems), and imaged using a FluoView FV3000 confocal laser scanning microscope (Olympus/Evident).

The following primary antibodies were used: goat anti-RFP (1:2000; Rockland, 200-101-379), guinea pig anti-Glut1 (1:1000; Frontier Institute, Af610), and/or rabbit anti-Sox9 (1:1000; Abcam, ab185966). Corresponding secondary antibodies included donkey anti-goat IgG conjugated to Cy™3 (1:1000; Jackson ImmunoResearch, 705-165-147), donkey

anti-guinea pig IgG conjugated to biotin (1:1000; Jackson ImmunoResearch, 706-066-148), and/or donkey anti-rabbit IgG conjugated to Alexa™647 (1:1000; Jackson ImmunoResearch, 711-606-152). Tomato lectin (1:1000; Vector Laboratories, FL-1171) was used for vascular endothelial staining.

For enhanced immunostaining using horseradish peroxidase (HRP), endogenous peroxidase activity was quenched by incubating sections in 1% H_2O_2 in PBS for 20 minutes after antigen retrieval, followed by PBS washes. The standard immunostaining protocol was then followed. After the secondary antibody incubation and subsequent washes, sections were incubated with the avidin–biotin–peroxidase complex using the VECTASTAIN Elite ABC Kit (Vector Laboratories, PK-6100) for 30 minutes and washed three times with PBST. HRP activity was visualized using Tyramide Signal Amplification (TSA) with Cyanine5 (1:500; PerkinElmer, FP1171).

In Fig. 1, Aldh1l1-CreERT2; tdTomato reporter mice were administered tamoxifen intraperitoneally at 100 mg/kg once daily for three consecutive days starting at P45. Brains were fixed and processed for immunostaining analysis three weeks after the final tamoxifen injection.

Plasmid construction for AAV production

The AAV expression vector, pAAV-CAG-hGLUT1-MycTag-T2A-mCherry-WPRE, was constructed by custom DNA synthesis (VectorBuilder). The hGLUT1 coding sequence corresponds to NM_006516.4 (Supplementary_Table_1).

AAV Production and Purification

pAAV-BR1 was generated by inserting the 7-amino acid peptide NRGTEWD between positions 588 and 589 of the AAV2 capsid[36], along with an N587Q substitution (asparagine to glutamine). Similarly, pAAV-X1.1 was generated by inserting the 7-amino acid peptide DGAATKN between positions 588 and 589 of the AAV9 capsid[37,57]. The production of pAAV-AST is described in results.

HEK293T cells were cultured in standard medium (D-MEM supplemented with 10% heat-inactivated fetal bovine serum [hiFBS] and 1% penicillin–streptomycin [PS]) until reaching approximately 90% confluency. The cells were triple-transfected using polyethylenimine (PEI-Max) to produce AAV vectors, following the protocol described by Grieger et al[58]. (2006). Briefly, the transgene expression plasmid (pAAV-CAG-hGLUT1-MycTag-T2A-mCherry-WPRE), a packaging plasmid (pAAV-AST, pAAV-BR1, or pAAV-X1.1), and the pHelper plasmid were diluted and mixed in Opti-MEM (Life Technologies) to allow for the formation of DNA-PEI complexes.

Six to twelve hours after transfection, the culture medium was replaced with D-MEM containing 2% hiFBS and 1% PS. Viral particles were harvested from the medium 7-10 days post-transfection. For viral recovery, the collected supernatant was mixed with a 5× AAV precipitation buffer (200 g PEG 8000 [Sigma-Aldrich] and 73.05 g NaCl in 500 mL H_2O) and

incubated at 4 °C for 2-3 hours, as described by Guo et al[59]. The mixture was then centrifuged at 3,000 × g for 30 minutes at 4 °C. The resulting PEG precipitate was resuspended in Dulbecco's PBS (D-PBS) and treated with SuperNuclease (Sino Biological) in the presence of 5 mM MgCl2 for 60 minutes to digest residual host cell DNA and RNA. The reaction was subsequently terminated by the addition of 6.5 mM EDTA.

Finally, the virus was purified using an iodixanol discontinuous gradient, as described by Zolotukhin et al[60]. Briefly, following centrifugation to remove cellular debris, the clarified supernatant was layered onto an iodixanol (OptiPrep) step gradient (15%, 25%, 40%, and 54%) in an Ultra-Clear tube (25 × 89 mm; Beckman). The gradient was ultracentrifuged at 28,000 rpm for 18 hours at 10 °C. Viral fractions were then collected from the bottom three-fourths of the 40% layer to the top one-fourth of the 54% layer (approximately 4-5 mL) using a 19G needle. The eluate was buffer-exchanged and concentrated from PBS to HBSS using a Vivaspin 100K centrifugal filter (Sartorius).

AAV purity was evaluated by SDS-PAGE, and viral genome titers were quantified by qPCR using the KAPA SYBR Fast qPCR Kit (Nippon Genetics). Primers targeting the WPRE sequence were used:

- Forward: 5′-CTGTTGGGCACTGACAATTC-3′
- Reverse: 5′-GAAGGGACGTAGCAGAAGGA-3′

The expression plasmid served as the standard for quantification.

Peptide motif analysis

Selection of analyzed datasets: Four published AAV insertion library studies were analyzed. [30-33]. From Kumar et al., motifs showing $\log_{10}$ enrichment > 1 in GFAP-positive cells were extracted, clustered to remove near-identical variants, and representative sequences were selected. Together with five motifs from Nonnenmacher and one each from Kunze and Hanlon, these sequences comprised the reference motif set used to define the overall astrocyte/CNS-related motif landscape.

Extraction and normalization: Flanking residues derived from the VP3 587-590 loop (A-Q/A-Q) were trimmed, retaining only the 7-residue insertions between VP3 588-589 (pos1-pos7). The normalized 7-mer sequences were aligned to construct a position-frequency matrix (PFM) for visualization. Sequence logos were generated from the position-frequency matrix using a custom Python/Matplotlib script, with per-position letter heights scaled by information content.

Branch-aware motif compatibility scoring: Because several literature-derived astrocyte/CNS-related motifs converged on a limited set of closely related sequence branches, candidate prioritization was performed using a branch-aware motif compatibility score rather than a single pooled logo score. For candidate prioritization, four predefined PHP.B-like branches were used: TLAV-like, TALK-like, TTLK-like, and TLQx-like. The TLAV-like, TALK-like, TTLK-like, and TLQx-like branches were defined using representative motifs

centered on TLAVPFK, TALKPFL, TTLKPFL/TTLKPFS, and TLQLPFK/TLQQPFK/TLQIPFK-related sequences, respectively. For each branch, a branch-specific position-frequency model was constructed from normalized 7-mer motifs using Dirichlet pseudocount smoothing ($\alpha = 0.1$). Candidate sequences were scored against branch-specific position-frequency models using the mean log-likelihood across the seven positions, and the highest branch-specific value was retained as the branch-aware motif compatibility score. Scores were normalized to the top-ranked motif (= 1.0) for visualization and comparison.

Selection for in vivo validation: Candidate motifs ranked within the top-scoring group were prioritized for experimental testing. TLAVPFK was excluded because it is identical to the PHP.eB insertion sequence. TTLKPFL, TALKPFL, and TLQLPFK were therefore selected for in vivo validation.

***In vivo* administration of AAV-AST0, AAV-AST and AAV-AST3 in wild-type mice**
C57BL/6J mice at postnatal day 18 (P18) or 3 months of age received retro-orbital injections of AAV-AST0, AAV-AST, or AAV-AST3 at 3 × 10^11 viral genomes (vg) per mouse.

Cell culture, transfection and AAV transduction
Human brain microvascular endothelial cells (hBMECs; ACBRI 376) and the specialized complete medium kit with serum and CultureBoost (4Z0-500-R) were purchased from Cell Systems. Human cortical astrocytes (HAs; Cat. #1800) and Astrocyte Medium (AM; Cat. #1801) were obtained from ScienCell Research Laboratories. All cells were maintained at 37 °C in a humidified incubator with 5% CO_2.
For hBMEC culture, coverslips were pretreated with the attachment solution supplied by Cell Systems (4Z0-201) according to the manufacturer's instructions. Briefly, coverslips were incubated with the attachment solution, which was then recovered and reused. For human cortical astrocyte culture, plates or coverslips were coated overnight at 37 °C with poly-L-lysine (PLL; Sigma-Aldrich, P2636-100MG) at 1 μg μL^{-1} in Milli-Q water, washed three times with PBS and used for cell seeding.
For reporter assays in hBMECs (Fig. 5b,c) and human cortical astrocytes (Fig. 5d and Supplementary Fig. 4), cells were seeded in 24-well plates at densities of 20,000 cells per well and 22,800 cells per well, respectively, 24 h before transfection. Immediately before transfection, 250 μl of medium was removed from each hBMEC well. In astrocyte cultures, 250 μl of medium was temporarily collected and retained from each well before transfection. Cells were co-transfected with pAAV-hSLC2A1p-mCherry and pAAV-CAG-GFP at a 1:1 molar ratio, with a total of 500 ng DNA per well, using Lipofectamine LTX (Thermo Fisher Scientific, 15338100) according to the manufacturer's instructions. Negative-control wells received no transfection treatment. At 6 h after transfection, 250 μl of medium was added to each hBMEC well, whereas the retained medium was returned to each astrocyte well. Cells were fixed the following day with 4% paraformaldehyde, and nuclei were counterstained with Hoechst. No immunostaining was performed; mCherry and GFP fluorescence were evaluated directly.

For AAV transduction assays in human cortical astrocytes (Fig. 3d–f), cells were seeded in 24-well plates and maintained in monoculture. The indicated AAV vectors carrying a CAG-driven GFP reporter were added at 1×10^9 viral genomes (vg) per well. Cells were fixed 3 d after transduction, counterstained with Hoechst and subjected to fluorescence imaging.

Image acquisition and quantitative analysis

Fluorescence images were acquired using a BZ-X1000 microscope (Keyence) with a 10× objective lens and saved as 24-bit TIFF files. Quantitative image analysis was performed using custom Python scripts. For analysis, each fluorescence channel was processed separately using single-channel images converted to 8-bit grayscale prior to binarization, and all fixed thresholds were applied to 8-bit images (intensity range, 0–255). Within each experiment, identical analysis parameters were applied across all experimental groups. For each sample, five fields were randomly selected for analysis, excluding fields containing saturated signals or coverslip edges. Three independent experiments were performed on separate days for each condition. In assays using fixed thresholds, exposure time, gain, binning, and image size were kept constant within each assay. The analysis targets, binarization conditions, noise exclusion criteria, and quantitative metrics were defined for each experimental system as follows.

Quantification of AAV transduction efficiency in primary mouse astrocytes: GFP and Hoechst 33342 (Nacalai Tesque, 04929-82) fluorescence images were analyzed. Hoechst images were binarized using the IsoData method, and objects smaller than 10 pixels were excluded as noise. GFP images were binarized using a fixed threshold of 48. For each nucleus, the overlap between the Hoechst-derived nuclear mask and the GFP signal was calculated, and nuclei with a GFP-overlapping area covering at least 30% of the nuclear area were classified as GFP-positive. Transduction efficiency was calculated for each field as the number of GFP-positive nuclei divided by the total number of Hoechst-positive nuclei.

Quantification of hGLUT1 promoter activity in hBMECs: GFP and mCherry fluorescence images were analyzed. Images were binarized using fixed thresholds (GFP, 28; mCherry, 49), and objects smaller than 30 pixels were excluded as noise. The number of valid objects detected after binarization was counted for each channel, and promoter activity was quantified for each field as the ratio of mCherry-positive objects to GFP-positive objects.

Quantification of hGLUT1 assay (AAV transduction) in iPSC-derived astrocyte :

mCherry and Hoechst fluorescence images were analyzed. Images were binarized using fixed thresholds (Hoechst, 17; mCherry, 18), and nuclear objects smaller than 10 pixels were excluded as noise. For each nucleus, the overlap between the Hoechst-derived nuclear mask and the mCherry signal was calculated, and nuclei with an mCherry-overlapping area covering at least 30% of the nuclear area were classified as mCherry-positive. Expression efficiency was calculated for each field as the number of mCherry-positive nuclei divided by the total number of Hoechst-positive nuclei.

Quantification of hGLUT1 promoter activity in primary human astrocytes: GFP and mCherry fluorescence images were analyzed. Images were binarized using fixed thresholds (GFP, 10; mCherry, 15), and objects smaller than 100 pixels were excluded as noise. The number of valid objects detected after binarization was counted for each channel, and promoter activity was quantified for each field as the ratio of mCherry-positive objects to GFP-positive objects.

Construction of reporter plasmids

Reporter plasmids for subsequent recombinant adeno-associated virus (rAAV) production were constructed by fusing candidate promoter/enhancer elements to the mCherry reporter gene. Each expression cassette was flanked by inverted terminal repeat (ITR) sequences, and a woodchuck hepatitis virus posttranscriptional regulatory element (WPRE) was included to enhance transgene expression. Candidate cis-regulatory regions (regions a–i) were selected from the human SLC2A1 locus (chr1: 42,956,501–42,968,500; GRCh38/hg38) and amplified by PCR from human genomic DNA isolated from HEK293 cells. To generate reporter constructs, pAAV-CAG-mCherry-spacer-WPRE (Supplementary Table 2) or pAAV-CAG-mCherry-WPRE (derived from pAAV-CAG-mCherry-spacer-WPRE by removal of the spacer sequence) was digested with XbaI and XhoI to produce a linearized backbone containing the mCherry reporter, WPRE, and ITR sequences. Promoter/enhancer fragments were then inserted upstream of mCherry within the ITR-flanked expression cassette using NEBuilder HiFi DNA Assembly Master Mix (New England Biolabs, E2621). Regulatory elements a, b, c, d, e, f and f k were cloned into pAAV-promoterless-mCherry-spacer-WPRE, whereas regulatory elements f, g, h, and i were cloned into pAAV-promoterless-mCherry-WPRE. For constructs containing regulatory elements a, b, c, e, f, and g, putative ATG sequences were removed by site-directed mutagenesis PCR after plasmid assembly. Primer sequences and primer names are provided in Supplementary Table 3.. The resulting plasmids were transformed into Escherichia coli DH5α competent cells (Takara Bio, 9057) and purified using a NucleoBond Xtra Midi kit (Takara Bio, 740410). A plasmid expressing GFP under the control of the CAG promoter was used as an internal control.

Imaging and Statistical Analysis

Fluorescence observation and quantitative analysis were performed using an FV3000 confocal laser scanning microscope, with all images captured under identical laser power and detection settings across all samples. For quantification, images captured with a Keyence BZ-X1000 microscope were analyzed using ImageJ software (NIH). Reporter activity was defined as the percentage of mCherry-positive cells exceeding a fixed fluorescence intensity threshold among the total GFP-positive cell population. Quantification was performed using 15 fields per condition from 3 independent experiments; field-level measurements were averaged within each experiment, and n represents independent experiments.

Administration of AAVs for Glut1 del/+ mice

AAVs were administered via the retro-orbital sinus[61] to Glut1 del/+ mice between P15 and P19. Mice were anesthetized using a combination of three agents: medetomidine (0.375 mg/kg; Nippon Zenyaku Kogyo Co., Ltd., Fukushima, Japan), midazolam (2 mg/kg; Maruishi Pharmaceutical Co., Ltd., Osaka, Japan), and butorphanol (2.5 mg/kg; Meiji Seika Pharma Co., Ltd., Tokyo, Japan). Glut1 del/+ mice received AAV-BR1, AAV-X1.1 and/or AAV-AST at doses of 1.0–7.5 × 10^{11} vg per mouse for each virus, diluted in 100 µL of Hanks' Balanced Salt Solution (HBSS) containing 0.5% Fast Green. Control littermates received 100 µL of vehicle (HBSS with 0.5% Fast Green) via the same retro-orbital injection method.

Culture of human iPSCs and generation of iPSC-derived astrocytes and EECM-derived brain microvascular endothelial cell-like cells

The WTC11 human iPSC line (Coriell Institute, GM25256), derived from a healthy male donor, was maintained on growth factor-reduced Matrigel (Corning) in mTeSR Plus medium (STEMCELL Technologies) supplemented with 1% penicillin-streptomycin (Nacalai Tesque) at 37°C in a humidified incubator with 5% CO_2. The medium was changed every other day, and cells were passaged at approximately 80% confluence. For passaging, cells were dissociated with Accutase (Nacalai Tesque) at 37°C for 5 min. For low-density plating, 10 µM Y-27632 (Fujifilm Wako Pure Chemical) was added to the culture medium.
A total of 1.0 × 10^6 human iPSCs were resuspended in DMEM/F-12 with GlutaMAX (Gibco) supplemented with 2% B-27 without vitamin A (Gibco), 1% N-2 supplement (Gibco), 10 µM SB431542 (Fujifilm Wako Pure Chemical), 0.1 µM LDN193189 (Tocris Bioscience), 10 µM Y-27632, and 1% penicillin-streptomycin, and cultured in suspension in 25-cm^2 flasks (TPP) for 5 days to induce neurosphere formation.
Neurospheres were then plated onto plates sequentially coated with poly-L-ornithine (Fujifilm Wako Pure Chemical) and laminin (Gibco). When the cultures reached approximately 90% confluence, cells were passaged at a 1:2 ratio and maintained in DMEM/F-12 with GlutaMAX supplemented with 2% B-27 without vitamin A, 1% N-2 supplement, 20 ng/mL FGF2 (PeproTech), 10 µM Y-27632, and 1% penicillin-streptomycin to generate neural progenitor cells (NPCs). After 8 days of culture, neural rosette-like structures were observed.
NPCs (1.45 × 10^5 cells) were subsequently replated onto Matrigel-coated plates and differentiated into astrocytes by culture in Astrocyte Medium (ScienCell) for 30 days^54. From day 31 onward, cells were maintained in Astrocyte Medium without astrocyte growth supplement (AGS; ScienCell). For passaging of both NPCs and astrocytes, cells were dissociated with Accumax (Innovative Cell Technologies) at 37°C for 5 min.

For generation of EECM-derived brain microvascular endothelial cell-like cells (EECM-BMEC-like cells), we used two healthy control hiPSC lines, HPS1006 and HPS4290, originally established from healthy donors (36-year-old male and 36-year-old female, respectively) as previously reported[62]. These lines were obtained from the RIKEN BioResource Research Center (RIKEN BRC) through the National BioResource Project of MEXT/AMED, Japan. hiPSCs were cultured on growth factor-reduced Matrigel-coated plates in mTeSR1 medium (STEMCELL Technologies) under standard humidified conditions at

37°C with 5% CO_2. The culture medium was refreshed daily. Cells were passaged when they reached approximately 80% confluence. For routine passage, colonies were detached using ReLeSR (STEMCELL Technologies) according to the manufacturer's instructions and transferred onto newly Matrigel-coated plates.

EECM-BMEC-like cells were generated from hiPSCs using the extended endothelial cell culture method (EECM), with minor modifications from our previous reports[63-65]. Briefly, endothelial differentiation was induced by CHIR99021, and CD31-positive cells were isolated by magnetic-activated cell sorting and plated on collagen-coated dishes. Endothelial cells were further purified by repeated brief Accutase treatment based on their preferential detachment from contaminating smooth muscle-like cells. The resulting EECM-BMEC-like cells were used at passages 3–6 and maintained in endothelial maintenance medium (hECSR; human endothelial SFM supplemented with B-27 and 20 ng/mL FGF2) with medium changes every other day.

AAV transduction assay in iPSC-derived astrocytes and EECM-BMEC-like cells

Human iPSC-derived astrocytes (Fig. 6C,D) were seeded at 1 × 10^4 cells per well onto 13-mm coverslips (MATSUNAMI) placed in 24-well plates. Coverslips were coated with growth factor-reduced, phenol red-free Matrigel Matrix (Corning) at 37°C for 1 h. Cells were seeded at differentiation day 34 and maintained in Astrocyte Medium without astrocyte growth supplement (AGS). Twenty-four hours after seeding (day 35), AAV-AST vectors carrying Region Ref., Region d, or Region d upstream of the mCherry were added at 1 × 10^10 viral genomes (vg) per well. Cells were fixed 6 days after transduction and counterstained with Hoechst before fluorescence imaging.

Human iPSC-derived EECM-BMEC-like cells (Fig. 6E) were seeded at 2,500 cells per well in collagen-precoated 384-well plates (Corning) and cultured in hECSR medium. Twenty-four hours later, AAV-X1.1 vectors carrying Region Ref., Region d, or Region d upstream of the mCherry were added at 5 × 10^9 viral genomes (vg) per well. Live-cell images were acquired 8 days after transduction using a BZ-X810 microscope (KEYENCE, Osaka, Japan) at ×20 magnification. To reduce potential selection bias, images were automatically captured at the center of each well as reported previously66.

For fluorescence quantification in the EECM-BMEC-like cell assay, one image was automatically acquired from the center of each well, and 12 wells were analyzed per experiment. mCherry signal was quantified using the BZ-X800 Analyzer software (KEYENCE) as R (integrated), defined as the sum of red-channel pixel intensities within the analyzed image area. Because this value reflects integrated fluorescence intensity rather than an absolute physical quantity, data are presented in arbitrary units (a.u.).

Statistics

Statistical analyses are described in the figure legends. All analyses were performed using GraphPad Prism 10 (GraphPad Software). The number of animals used for each experiment/analysis can be found in each figure legend.

Data availability statement

All data supporting the findings of this study are available within the paper and its supplementary information files. Additional data are available from the corresponding author upon reasonable request.

Acknowledgments

We thank Dr. T. Hara (TMiMS, Tokyo, Japan) for kindly sharing Tie2-Cre mice. We are also grateful to Dr. M. Murakami (The University of Tokyo, Tokyo, Japan) for generously providing CAG-Cre mice, originally generated by Dr. J. Miyazaki (Osaka University, Suita, Japan). We further thank Dr. M. Hasegawa (TMiMS, Tokyo, Japan) and Dr. A. Nagakura (Tokyo Metropolitan Matsuzawa Hospital, Tokyo, Japan) for coordinating the acquisition and distribution of postmortem brain samples. Finally, we express our deepest gratitude to the families of the deceased individuals for their generous donation of brain tissue and for their time and cooperation during the consent and interview process.

Funding

This work was supported by the JST FOREST Program (JPMJFR2169 to S.H.);
the Food Science Institute Foundation (Ryoushoku-kenkyukai);
the Takeda Science Foundation;
the Naito Foundation (to S.H.); and
the Ichiro Kanehara Foundation (to S.T.).

Author contributions

S.H. designed the study. S.T., H.S., N.A., Y.Y., A.S., K.M., H.N., E.S., K.S. and S.H. performed experiments. S.T., H.N., and S.H. performed data and image analysis. Y.M. and K.S. provided critical input on assay in iPSC-derived astrocytes and immunostaining of postmortem brain, respectively. S.T. wrote the first draft of the manuscript. S.T., H.S., N.A., and H.N. wrote the manuscript for methods. H.O. and S.H. edited the manuscript. S.H. supervised this study.

Figure 1

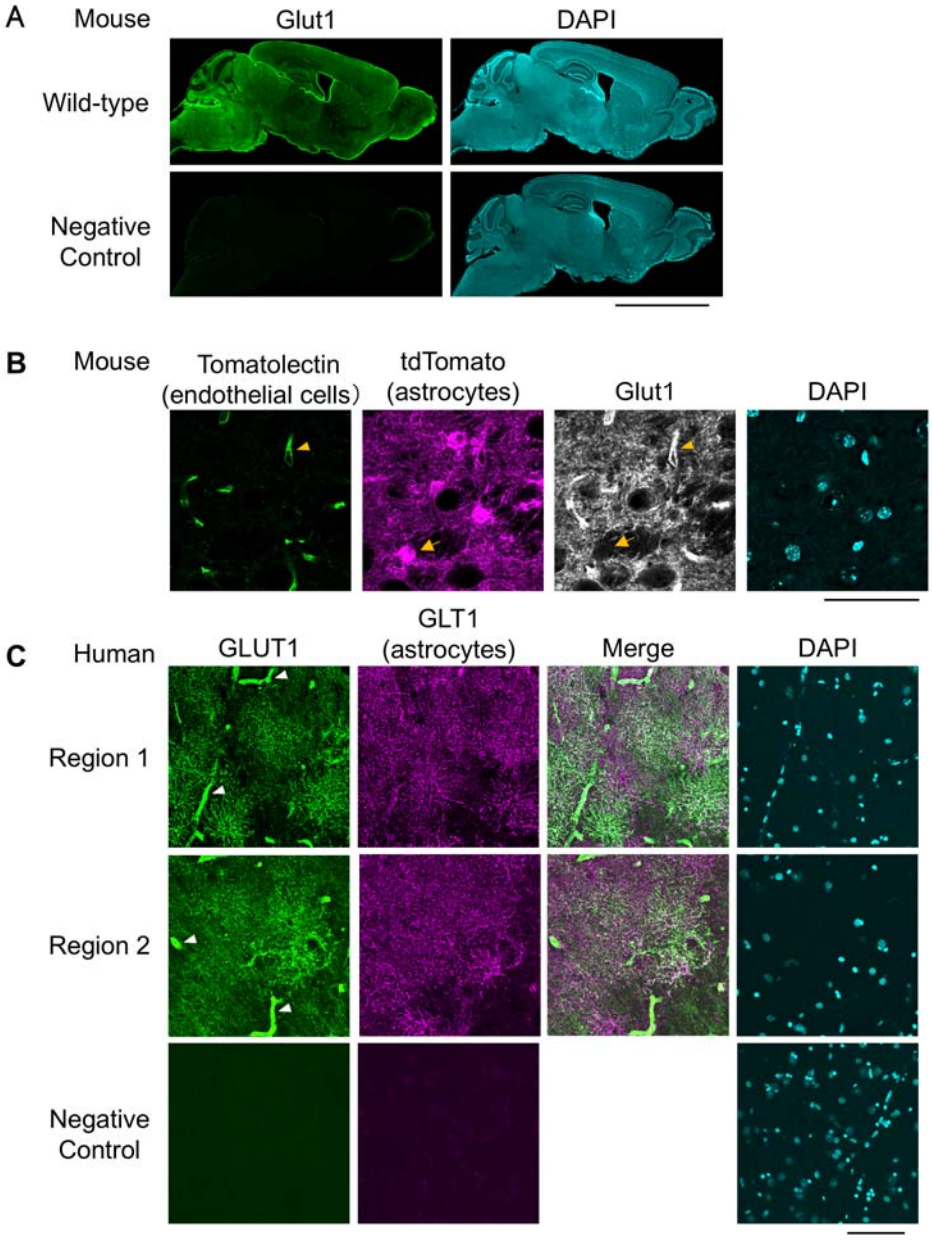
A
Mouse
Glut1
DAPI
Wild-type
Negative Control
B
Mouse
Tomatolectin (endothelial cells)
tdTomato (astrocytes)
Glut1
DAPI
C
Human
GLUT1
GLT1 (astrocytes)
Merge
DAPI
Region 1
Region 2
Negative Control

Figure 1. Glut1/GLUT1 expression in mouse and human brain.

(A) Representative sagittal brain sections from wild-type mice immunostained for Glut1 (green) and counterstained with DAPI (cyan). Negative control sections were processed in parallel without the primary anti-Glut1 antibody. Scale bar, 5 mm.(B) High-magnification images of the thalamic ventral posteromedial nucleus (VPM) from 2-month-old Aldh1l1-CreERT2; Rosa26^LSL-tdTomato (flex tdTomato) mice. Endothelial cells were labeled with tomato lectin (green), astrocytes with tdTomato (magenta), Glut1 immunoreactivity is shown in grayscale, and nuclei are counterstained with DAPI (cyan). Yellow arrowheads indicate Glut1 signal associated with lectin-positive vessels, and yellow arrows indicate Glut1 signal in tdTomato-positive astrocyte somata. Scale bar, 50 μm. (C) Representative images from normal human hippocampus stained for GLUT1 (green) and the astrocytic marker GLT1 (magenta), with merged images and DAPI (cyan). White arrowheads indicate vascular GLUT1 staining. Region 1 and Region 2 correspond to the stratum oriens (or alveus) and the pyramidal cell layer, respectively. Negative control sections were processed without primary antibodies. Scale bar, 50 μm. Glut1/GLUT1 immunostaining was visualized using tyramide signal amplification (TSA).

Figure 2

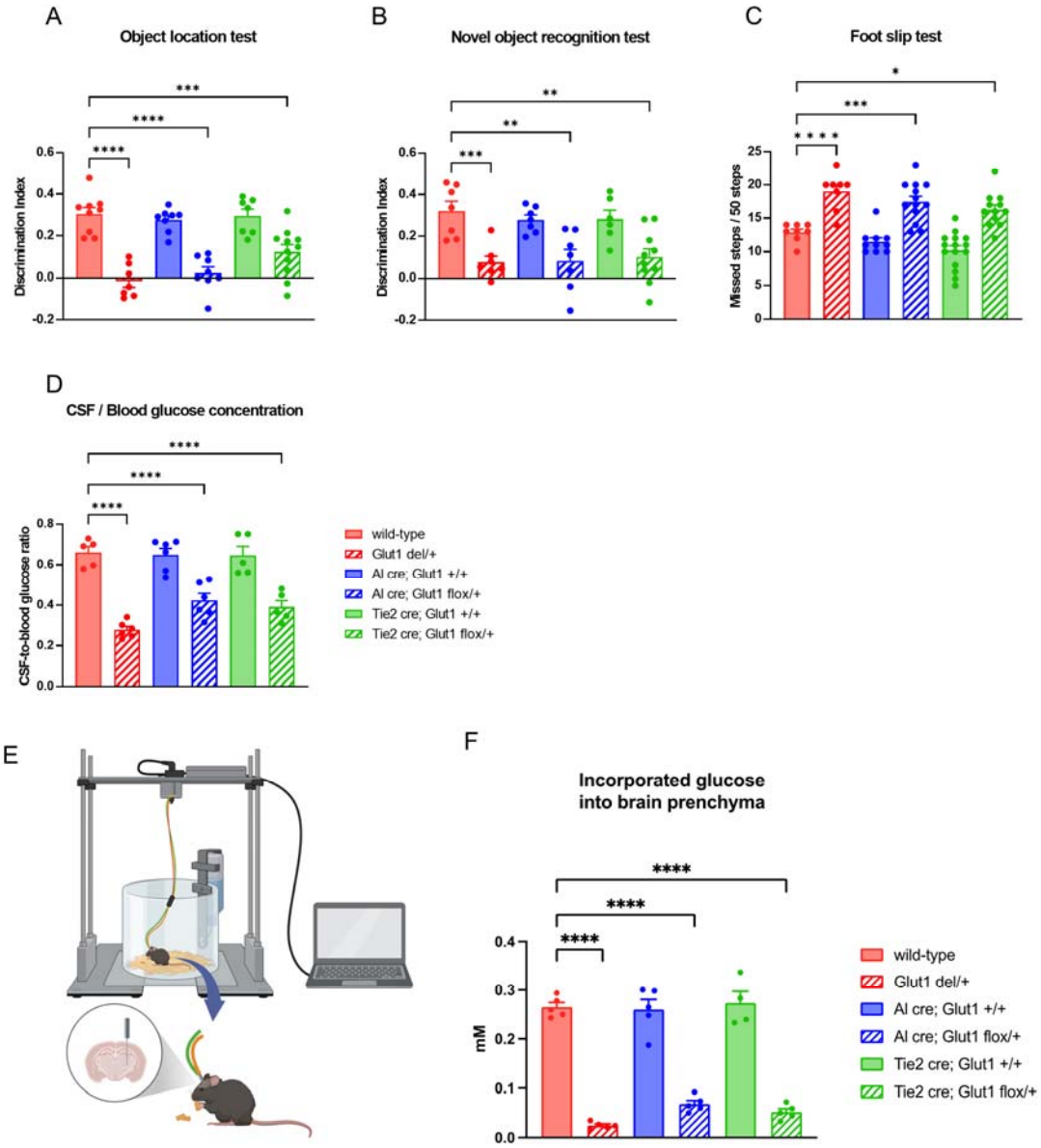
A
Object location test
Discrimination Index
B
Novel object recognition test
Discrimination Index
C
Foot slip test
Missed steps / 50 steps
D
CSF / Blood glucose concentration
CSF-to-blood glucose ratio
wild-type
Glut1 del/+
Al cre; Glut1 +/+
Al cre; Glut1 flox/+
Tie2 cre; Glut1 +/+
Tie2 cre; Glut1 flox/+
E
F
Incorporated glucose
into brain prenchyma
mM
wild-type
Glut1 del/+
Al cre; Glut1 +/+
Al cre; Glut1 flox/+
Tie2 cre; Glut1 +/+
Tie2 cre; Glut1 flox/+

Figure 2. Astrocyte- and endothelial-specific Glut1 haploinsufficiency recapitulates key features of GLUT1 deficiency syndrome.

(A–C) Behavioral analyses in six groups: wild-type, systemic Glut1 del/+ mice, Aldh1l1-Cre (Al cre); Glut1 +/+ mice, Al cre; Glut1 flox/+ mice, Tie2-Cre; Glut1 +/+ mice, and Tie2-Cre; Glut1 flox/+ mice (n = 6-15 mice per group). (A) Object location test (OLT) and (B) novel object recognition test (NORT) were used to assess spatial and recognition memory (discrimination index). (C) The foot-slip test evaluated motor coordination (missed steps per 50 steps). (D) CSF-to-blood glucose ratio measured in the same cohorts (n = 5-6 mice per group). Blood glucose levels were comparable across groups (see Supplementary Fig. 1). (E) Schematic of the *in vivo* recording setup for thalamic interstitial fluid (ISF) glucose measurement. Illustration created with BioRender. (F) ISF glucose measured following oral glucose administration (0.03 g per mouse, gavage). The increase in ISF glucose was markedly blunted in systemic, astrocyte-specific, and endothelial-specific Glut1 haploinsufficient mice compared with wild-type controls (n = 4-5 mice per group). Data are presented as mean ± SEM; dots represent individual mice. Statistical significance was determined by one-way ANOVA followed by Dunnett's multiple-comparison test (*$p < 0.05$, **$p < 0.01$, ***$p < 0.001$, ****$p < 0.0001$).

Figure 3

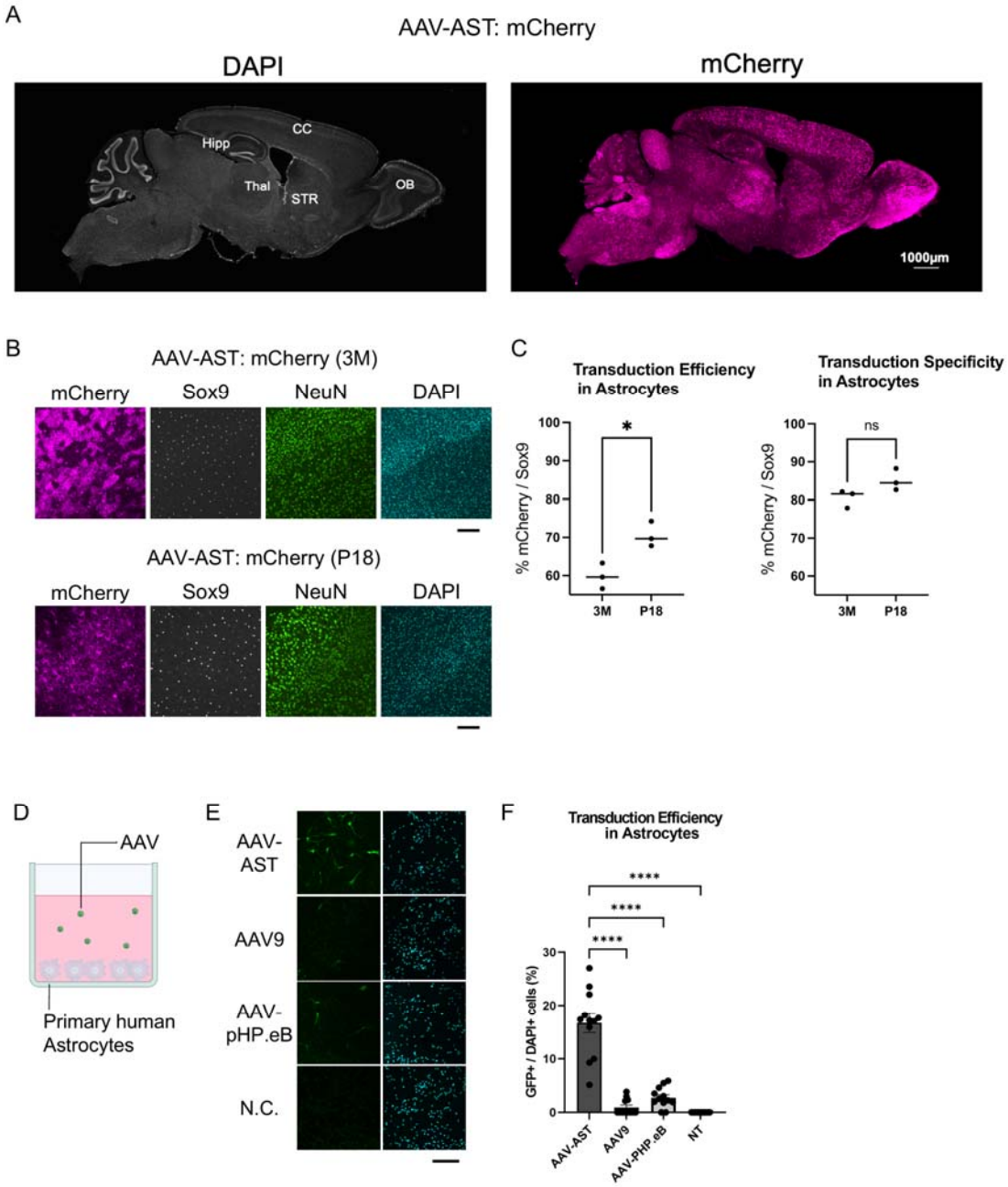
A
AAV-AST: mCherry
DAPI
mCherry
CC
Hipp
Thal
STR
OB
1000µm
B
AAV-AST: mCherry (3M)
mCherry
Sox9
NeuN
DAPI
AAV-AST: mCherry (P18)
mCherry
Sox9
NeuN
DAPI
C
Transduction Efficiency in Astrocytes
% mCherry / Sox9
100
90
80
70
60
*
3M
P18
Transduction Specificity in Astrocytes
% mCherry / Sox9
100
90
80
70
60
ns
3M
P18
D
AAV
Primary human Astrocytes
E
AAV-AST
AAV9
AAV-pHP.eB
N.C.
F
Transduction Efficiency in Astrocytes
GFP+ / DAPI+ cells (%)
30
20
10
0
****
****
****
AAV-AST
AAV9
AAV-PHP.eB
NT

Figure 3. Astrocyte-selective transduction of AAV-AST *in vivo* and *in vitro*.

(A) Representative sagittal brain sections showing mCherry expression (magenta) after retro-orbital administration of AAV-AST-CAG-mCherry into adult mice (3 months; 100 µL, 3.3 × 10^11 vector genomes (vg) per mouse). DAPI is shown in gray. Labeled regions: OB, olfactory bulb; CC, cerebral cortex; Thal, thalamus; STR, striatum; Hipp, hippocampus. Scale bar, 1,000 µm. (B) Representative immunofluorescence images of the somatosensory cortex 3 weeks after AAV administration at postnatal day 18 (P18) or 3 months (3M). mCherry (magenta), SOX9 (astrocytes, gray), NeuN (neurons, green), and DAPI (nuclei, cyan). Scale bar, 200 µm. (C) Quantification of astrocyte transduction efficiency (left; % of SOX9^+ cells expressing mCherry) and astrocyte specificity (right; % of mCherry^+ cells that are SOX9^+). Data are mean ± SEM (n = 3 mice per group). Two-sided Welch's t-test; *p < 0.05; ns, not significant. (D) Schematic of the in vitro astrocyte transduction assay using AAVs packaging a CAG-driven GFP reporter (CAG-GFP). Primary human astrocytes were cultured in monoculture, transduced with AAVs, and fixed 3 days later for fluorescence imaging. Created with BioRender.com. (E) Representative fluorescence images of astrocytes transduced with the indicated AAVs (GFP, green; DAPI, cyan). N.C., non-transduced control. Scale bar, 200 µm. (F) Quantification of astrocyte transduction efficiency corresponding to (E) (GFP^+/DAPI^+ cells, %). Data are mean ± SEM. Statistical significance was determined by one-way ANOVA followed by Tukey's multiple-comparison test (****p < 0.0001).

Figure 4

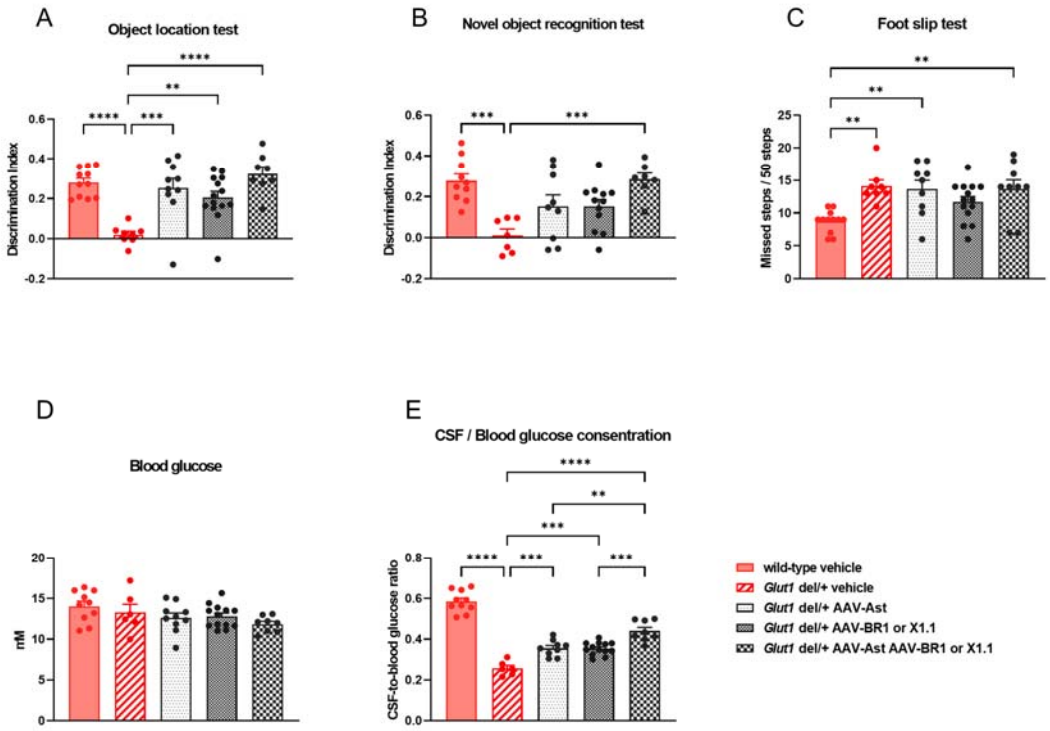

Figure 4. Cell-type–targeted AAV-Glut1 supplementation differentially rescues GLUT1-DS–like phenotypes.

(A–C) Behavioral analyses in five groups: wild-type + vehicle, Glut1 del/+ + vehicle, Glut1 del/+ + AAV-AST-Glut1 (astrocyte-targeted), Glut1 del/+ + AAV-BR1 (or X1.1)-Glut1 (endothelial-targeted), and Glut1 del/+ + AAV-AST-Glut1 + AAV-BR1(or X1.1)-Glut1. AAVs were administered between postnatal days 15 and 19 (P15-P19) via retro-orbital injection, and behavioral testing was performed starting at P48 (n = 5-14 mice per group). (A) Object location test (OLT) and (B) novel object recognition test (NORT) were used to assess memory performance (discrimination index). (C) Foot-slip test evaluated motor coordination (missed steps per 50 steps). (D, E) Blood glucose concentration (D) and CSF-to-blood glucose ratio (E) were measured (n = 6-14 mice per group). Data are presented as mean ± SEM; dots represent individual mice. Statistical significance was determined by one-way ANOVA followed by Tukey's multiple-comparisons test (****$p < 0.0001$, ***$p < 0.001$, **$p < 0.01$, *$p < 0.05$).

Figure 5

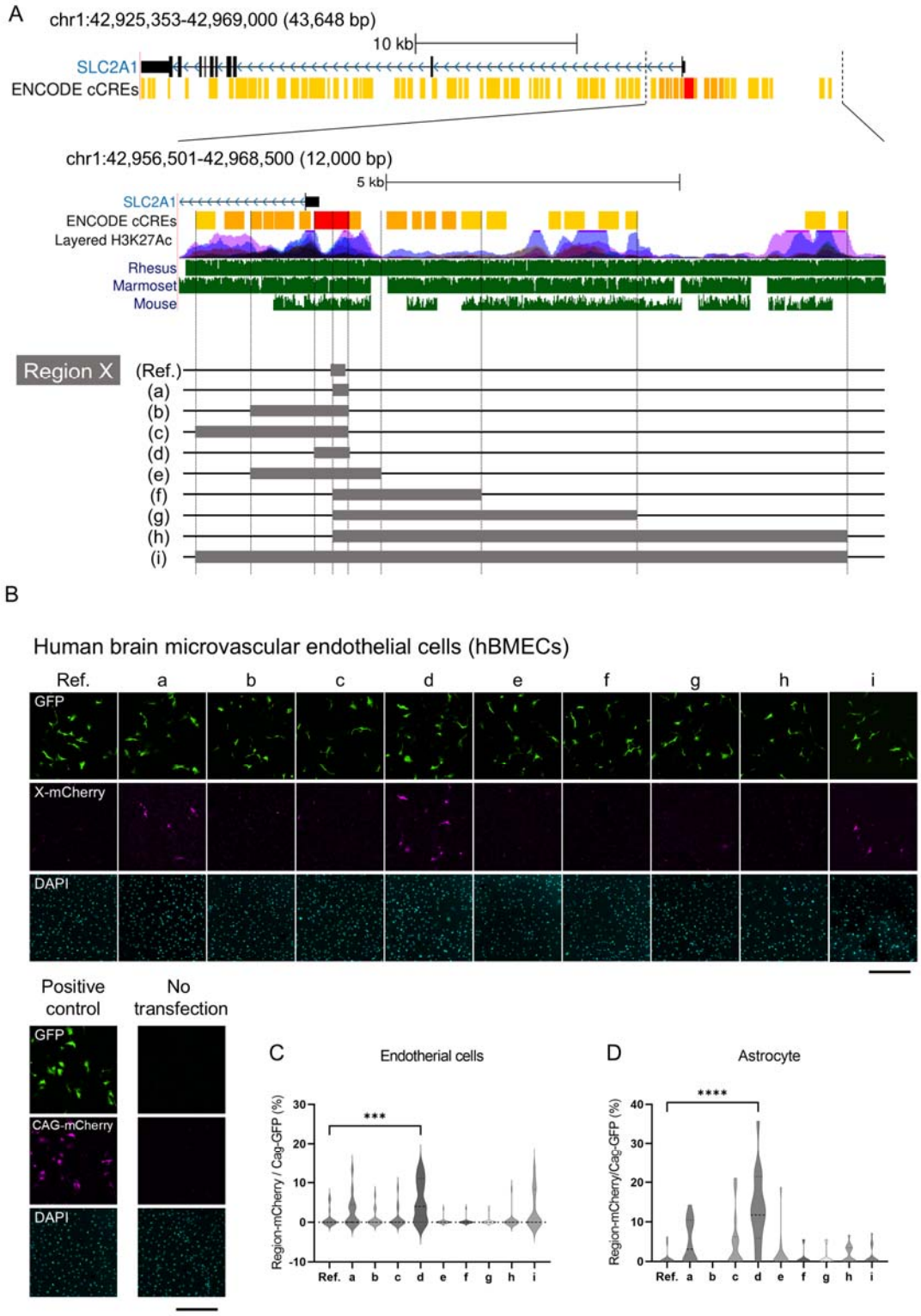
A
chr1:42,925,353-42,969,000 (43,648 bp)
10 kb
SLC2A1
ENCODE cCREs
chr1:42,956,501-42,968,500 (12,000 bp)
5 kb
SLC2A1
ENCODE cCREs
Layered H3K27Ac
Rhesus
Marmoset
Mouse
Region X
(Ref.)
(a)
(b)
(c)
(d)
(e)
(f)
(g)
(h)
(i)
B
Human brain microvascular endothelial cells (hBMECs)
Ref.
a
b
c
d
e
f
g
h
i
GFP
X-mCherry
DAPI
Positive control
No transfection
GFP
CAG-mCherry
DAPI
C
Endotherial cells
Region-mCherry / Cag-GFP (%)
***
D
Astrocyte
Region-mCherry/Cag-GFP (%)
****

Figure 5. Functional validation of predicted cis-regulatory regions at the human SLC2A1 locus.

(A) UCSC Genome Browser view of the human *SLC2A1* locus (GRCh38/hg38) showing ENCODE candidate cis-regulatory elements (cCREs; orange), layered H3K27ac enrichment (purple), and sequence conservation across rhesus, marmoset, and mouse (green). Gray boxes indicate predicted regulatory fragments (Ref. and Regions a-i) selected for functional testing and cloned upstream of an mCherry reporter (RegionX-mCherry). (B) Representative images of human brain microvascular endothelial cells (hBMECs) transfected with each RegionX-mCherry reporter (magenta) together with a CAG-GFP transfection control (green); nuclei were counterstained with DAPI (cyan). A CAG-mCherry plasmid served as a positive control for mCherry expression, and non-transfected cells served as a negative control. Scale bar, 300 µm. (C) Quantification of reporter activity in hBMECs, expressed as RegionX-mCherry/CAG-GFP (%) (n=3 independent experiments; 15 fields per experiment; violin plots with median and interquartile range (IQR; 25th–75th percentiles)). Statistical significance versus Ref. was assessed by one-way ANOVA followed by Dunnett's multiple-comparisons test (***$p < 0.001$). (D) Functional validation in primary cultured human astrocytes, performed as in (C). Reporter activity is shown as RegionX-mCherry/CAG-GFP (%) (n=3 independent experiments; 15 fields per experiment; violin plots with median and interquartile range (IQR; 25th-75th percentiles)). Statistical significance versus Ref. was assessed by one-way ANOVA followed by Dunnett's multiple-comparisons test (****$p < 0.0001$).

Figure 6

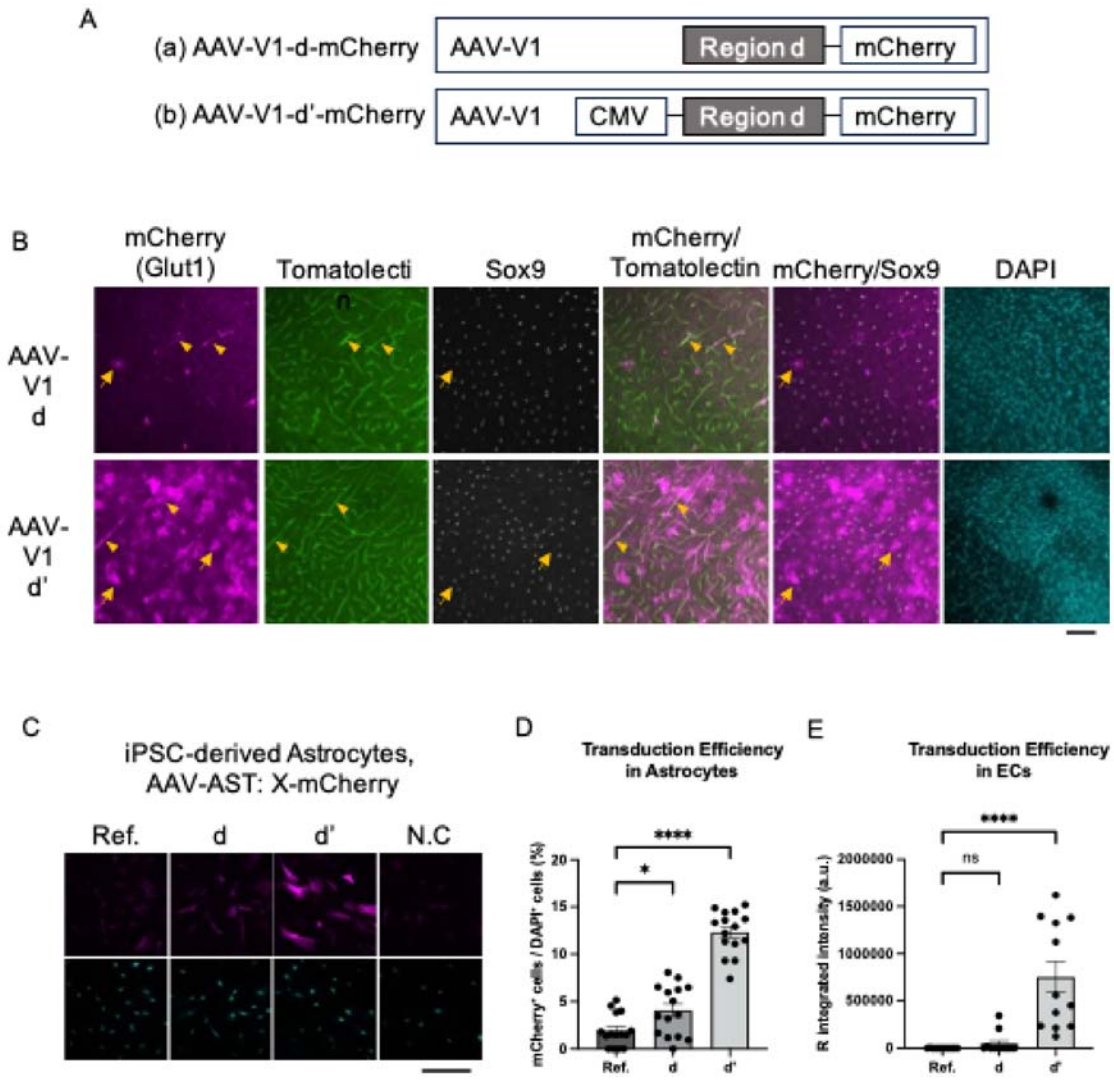

Figure 6. In vivo and in vitro validation of Region d regulatory activity using AAV vectors.

(A) Schematic of reporter constructs containing Region d, with or without an upstream CMV enhancer element, packaged into AAV-V1 capsids for in vivo analysis. (B) Representative confocal images of cortical sections from wild-type mice after retro-orbital administration of the indicated AAV-V1 vectors. mCherry is shown in magenta, tomato lectin marking vascular endothelial cells in green, SOX9 marking astrocytes in white, and DAPI in cyan. AAV-V1 carrying Region d alone drove reporter expression predominantly in vascular endothelial cells, with detectable expression in astrocytes. Addition of an upstream CMV enhancer to Region d (Region d) increased reporter signal without an obvious change in cell-type distribution. Yellow arrowheads indicate representative vascular endothelial cells,

and yellow arrows indicate astrocytes. Scale bar, 100 μm. (C) Representative fluorescence images of human iPSC-derived astrocytes transduced with AAV-AST vectors containing the indicated genomic regions (Ref., d, or d). mCherry, magenta; DAPI, cyan. N.C., non-transduced control. Scale bar, 300 μm. (D, E) Quantification of transduction in human iPSC-derived astrocytes (D) and human iPSC-derived endothelial cells (E). In astrocytes (D), transduction efficiency is expressed as the percentage of $mCherry^{+}/DAPI^{+}$ cells. In endothelial cells (E), mCherry signal was quantified as red-channel integrated fluorescence intensity (R, integrated; arbitrary units). Data are shown as mean ± SEM. Statistical significance was determined by one-way ANOVA followed by Tukey's multiple-comparison test (*$P < 0.05$, ***$P < 0.0001$).

Supplementary Fig.1

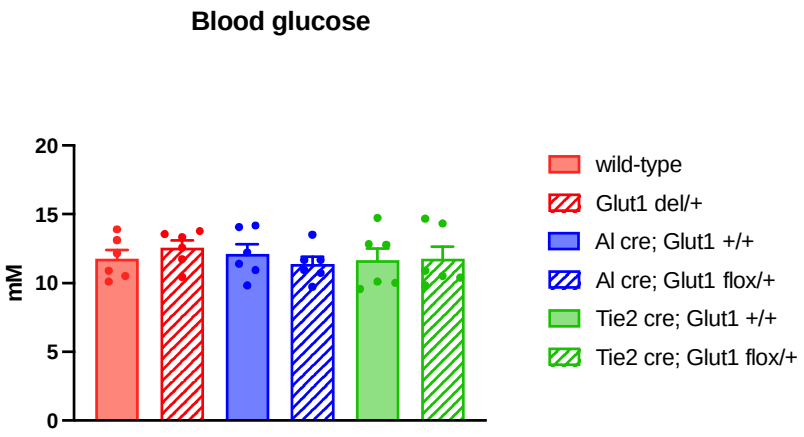

Supplementary Fig. 1 | Random-fed blood glucose in mice with cell type–specific Glut1 haploinsufficiency.

Random-fed (non-fasted) blood glucose concentrations in the indicated genotypes. Bars represent mean ± SEM (n = 6 mice per group). Statistical significance was assessed by one-way ANOVA followed by Tukey's multiple-comparisons test; no significant differences were observed among groups.

Supplementary Fig.2

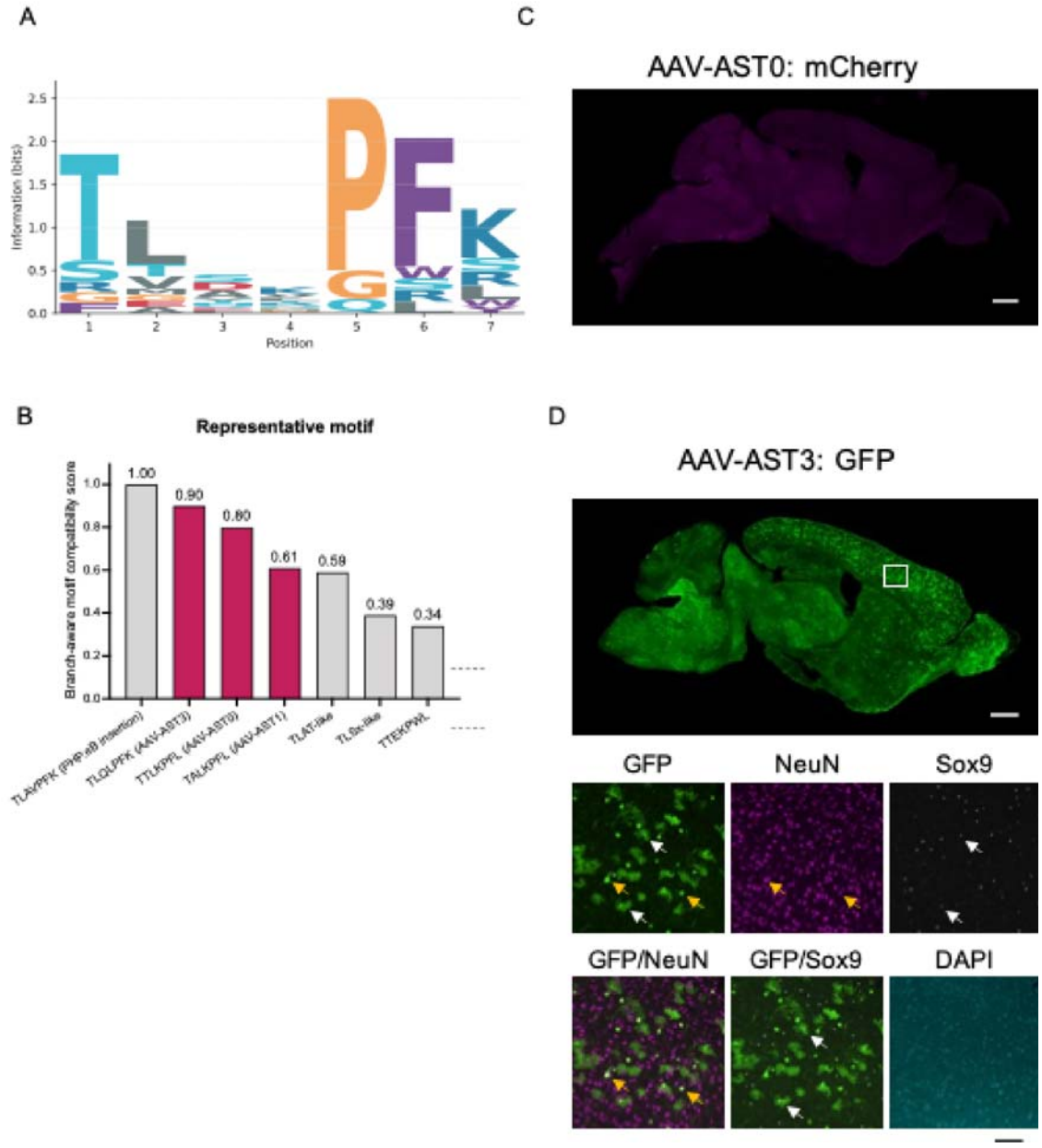

Supplementary Fig. 2 | Conserved motif structure and branch-aware ranking of astrocyte/CNS-related AAV insertions.

(A) Sequence logo representing the positional enrichment pattern of the normalized 7-mer reference motifs used to generate the position-frequency matrix (PFM). Enrichment was observed at Thr (position 1) and Pro-Phe (positions 5-6), delineating a T(L/A/T)xxPF[K/L] core architecture shared by astrocyte/CNS-related variants. (B) Branch-aware motif compatibility scores of representative astrocyte/CNS-related AAV insertion motifs. Four literature-supported PHP.B-like branches (TLAV-like, TALK-like, TTLK-like, and TLQx-like) were defined, and candidate sequences were scored against branch-specific position-frequency models. Scores were normalized to the top-ranked motif (= 1.0). For visualization,

near-identical motifs were collapsed and representative sequences are shown. TLAVPFK, TLQLPFK, TTLKPFL, and TALKPFL ranked within the top-scoring group, with TLAVPFK excluded from experimental testing because it is identical to the PHP.eB insertion sequence. (C, D) Representative sagittal brain sections following intravenous administration (retro-orbital injection) of AAV-AST0:CAG-mCherry (C) and AAV-AST3:CAG-GFP (D) into 3-month-old mice (100 μL, 3.3 × 10^11 vg per mouse). Scale bars, 1,000 μm. Enlarged views in (D) show immunostaining for GFP together with NeuN and SOX9. White and yellow arrows indicate representative SOX9-positive astrocytes and NeuN-positive neurons colocalized with GFP signals, respectively. Scale bars, 100 μm.

Supplementary Fig. 3

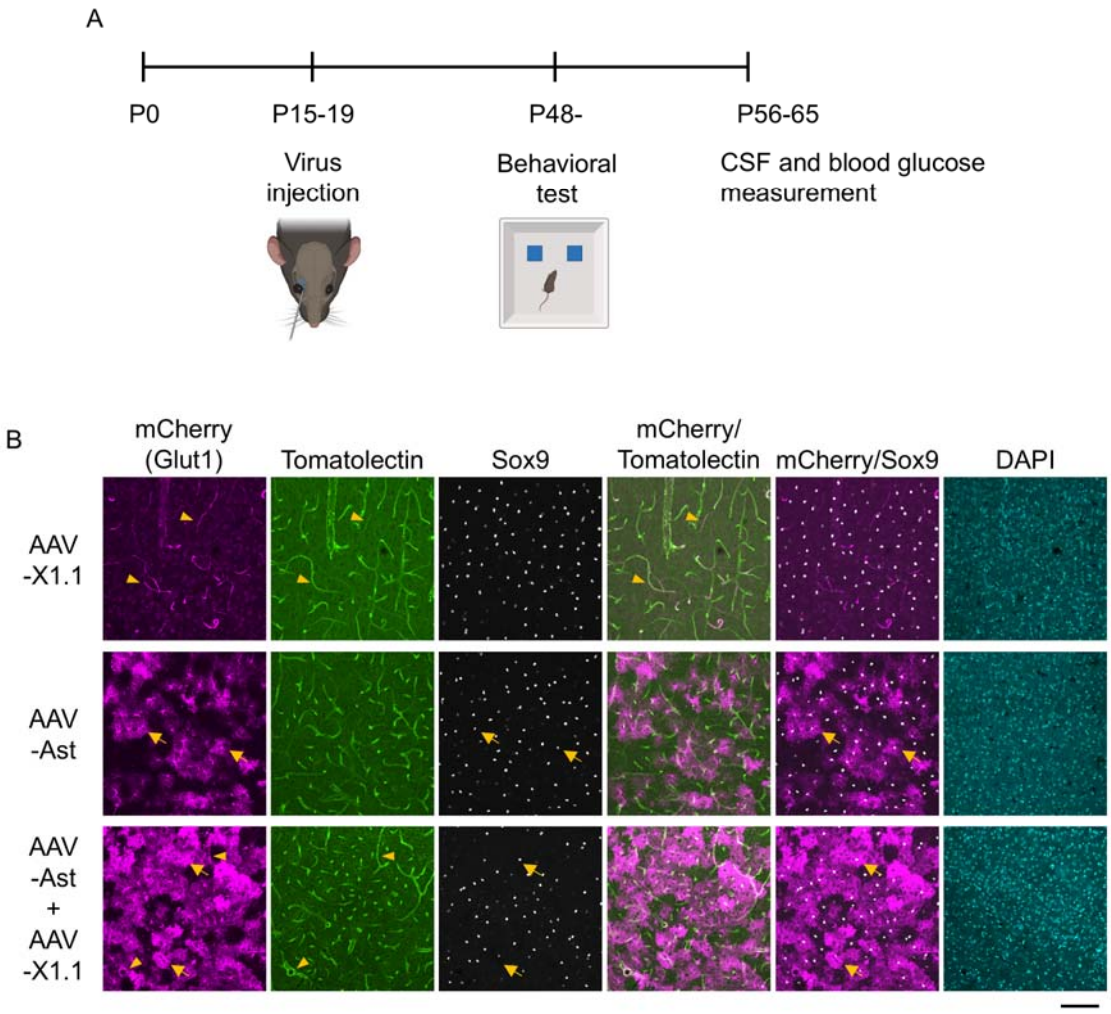

Supplementary Fig. 3 | Cell-type–specific Glut1 supplementation in Glut1 haploinsufficient mice via AAV administration.

(A) Experimental workflow for Glut1 supplementation using AAV. The illustration was created with BioRender. (B) Representative transgene expression after intravenous delivery of AAV-X1.1 (EC-targeting), AAV-AST (astrocyte-targeting), or AAV-AST + AAV-X1.1 (dual targeting) in Glut1 haploinsufficient mice. Representative confocal z-stack maximum-intensity projections were acquired from the cortex of Glut1 haploinsufficient mice injected with AAV. mCherry is shown in magenta, lectin in green, SOX9 in white, and DAPI in cyan. Yellow arrows and arrowheads indicate representative astrocytes and ECs colocalized with mCherry, respectively. Scale bar, 100 μm.

Supplementary Fig. 4

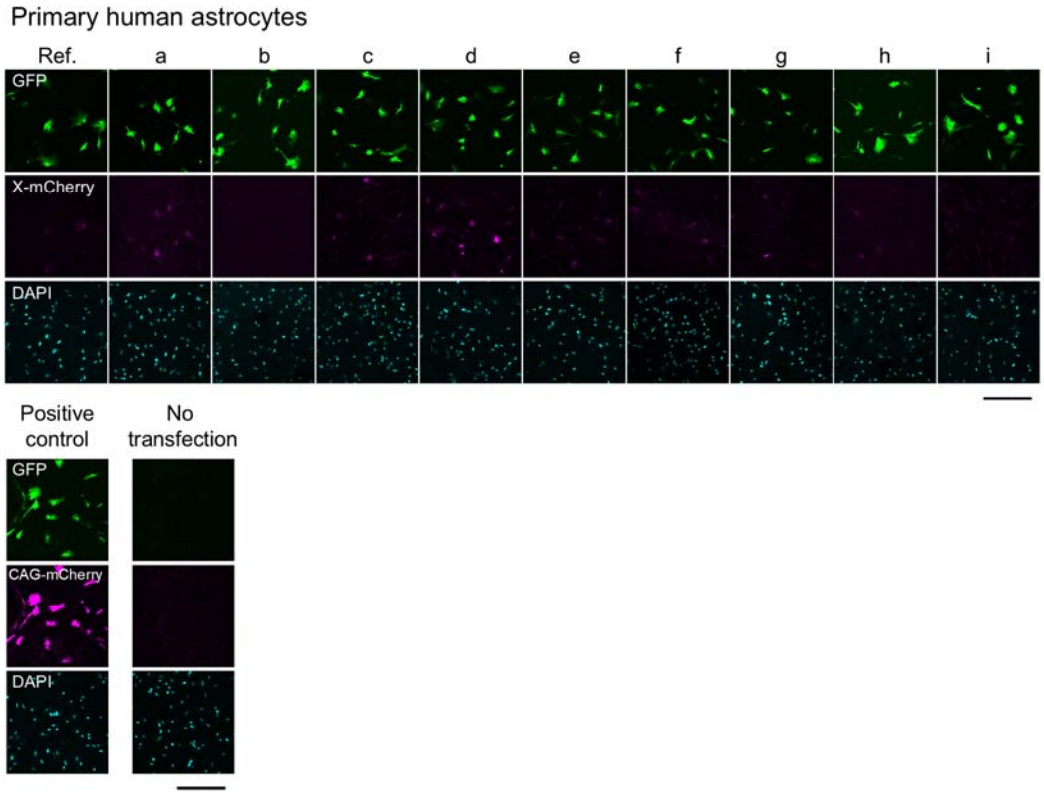

Supplementary Fig. 4 | Functional validation of human SLC2A1 regulatory regions in primary human astrocytes.

Reporter constructs containing candidate SLC2A1 regulatory regions (a-i) upstream of mCherry were transfected into primary cultured human astrocytes. CAG-GFP was co-transfected to monitor transfection efficiency in all conditions, except for the non-transfected negative control. As a positive control, CAG-mCherry was co-transfected with CAG-GFP. GFP is shown in green, mCherry in magenta, and DAPI in cyan. Scale bar, 300 μm.

Supplementary Fig. 5

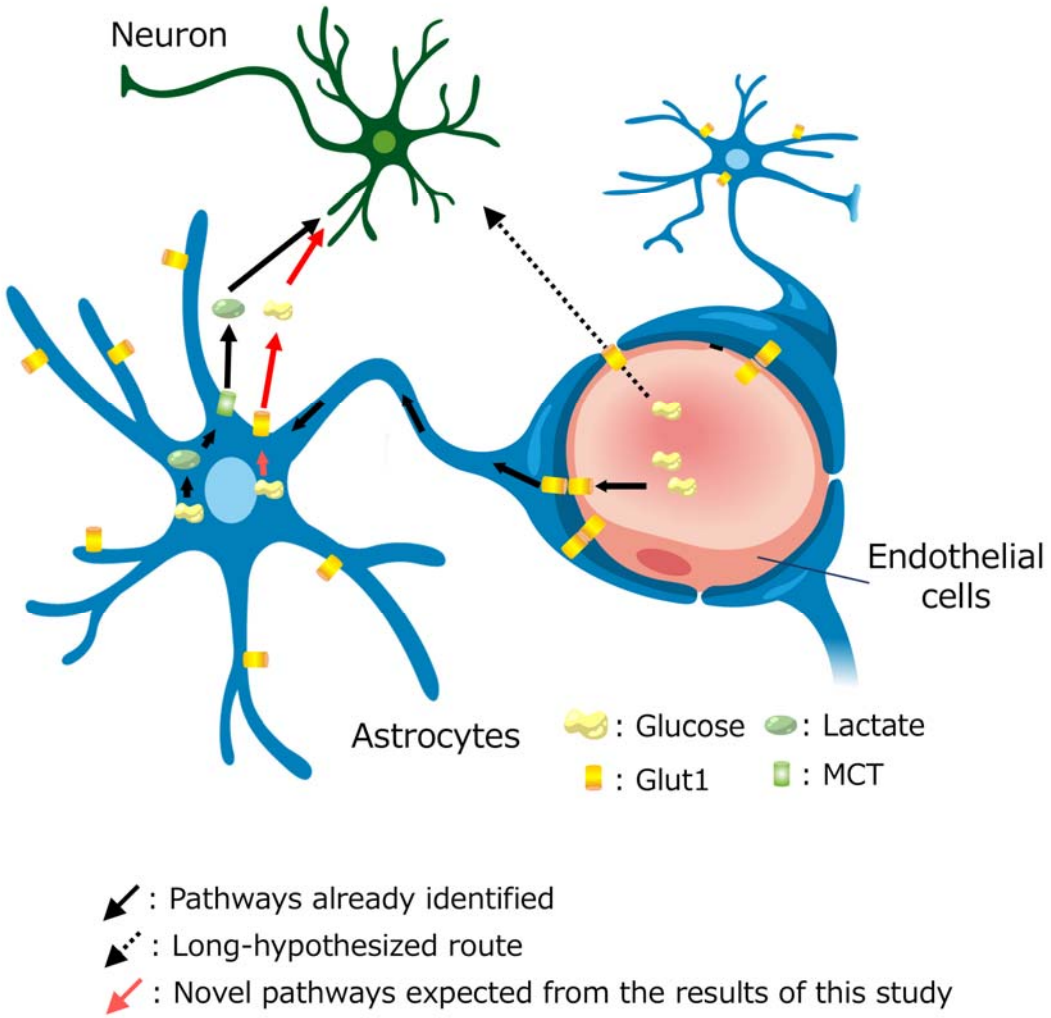

Supplementary Fig. 5 | Model: astrocytic and endothelial GLUT1 form a "two-cell gateway" contributing to glucose homeostasis in the brain parenchyma and cerebrospinal fluid (CSF).

Endothelial GLUT1 mediates glucose transport across the blood–brain barrier (BBB). Astrocytic GLUT1, distributed from perivascular endfeet to distal processes, may contribute to maintaining glucose availability within the parenchyma and CSF. Haploinsufficiency of GLUT1 in either compartment is associated with reduced CSF and interstitial fluid (ISF) glucose levels and with cognitive and motor impairments, whereas phenotypic rescue in our experiments required restoration of GLUT1 in both endothelial and astrocytic compartments, consistent with this model. Astrocytes can further metabolize glucose into lactate and supply it to neurons via the astrocyte–neuron lactate shuttle[2,25,26]. Thus, astrocytes may act as central metabolic regulators that shape intracerebral concentration gradients of two major energy substrates—glucose and lactate.

Reference

1. Magistretti, P.J. & Allaman, I. A cellular perspective on brain energy metabolism and functional imaging. *Neuron* **86**, 883–901 (2015).
2. Bonvento, G. & Bolaños, J.P. Astrocyte-neuron metabolic cooperation shapes brain activity. *Cell Metab* **33**, 1546–1564 (2021).
3. Thorens, B. & Mueckler, M. Glucose transporters in the 21st Century. *Am J Physiol Endocrinol Metab* **298**, E141–145 (2010).
4. Veys, K., *et al.* Role of the GLUT1 Glucose Transporter in Postnatal CNS Angiogenesis and Blood-Brain Barrier Integrity. *Circ Res* **127**, 466–482 (2020).
5. Maher, F., Vannucci, S.J. & Simpson, I.A. Glucose transporter proteins in brain. *Faseb j* **8**, 1003–1011 (1994).
6. De Vivo, D.C., *et al.* Defective glucose transport across the blood-brain barrier as a cause of persistent hypoglycorrhachia, seizures, and developmental delay. *N Engl J Med* **325**, 703–709 (1991).
7. Leen, W.G., *et al.* Glucose transporter-1 deficiency syndrome: the expanding clinical and genetic spectrum of a treatable disorder. *Brain* **133**, 655–670 (2010).
8. López-Rivera, J.A., *et al.* A catalogue of new incidence estimates of monogenic neurodevelopmental disorders caused by de novo variants. *Brain* **143**, 1099–1105 (2020).
9. Symonds, J.D., *et al.* Incidence and phenotypes of childhood-onset genetic epilepsies: a prospective population-based national cohort. *Brain* **142**, 2303–2318 (2019).
10. Klepper, J., *et al.* Glut1 Deficiency Syndrome (Glut1DS): State of the art in 2020 and recommendations of the international Glut1DS study group. *Epilepsia Open* **5**, 354–365 (2020).
11. Takahashi, S., *et al.* The role of molecular analysis of SLC2A1 in the diagnostic workup of glucose transporter 1 deficiency syndrome. *J Neurol Sci* **416**, 117041 (2020).
12. Leen, W.G., *et al.* Cerebrospinal fluid analysis in the workup of GLUT1 deficiency syndrome: a systematic review. *JAMA Neurol* **70**, 1440–1444 (2013).
13. Ruiz Herrero, J., *et al.* Classic Ketogenic Diet and Modified Atkins Diet in SLC2A1 Positive and Negative Patients with Suspected GLUT1 Deficiency Syndrome: A Single Center Analysis of 18 Cases. *Nutrients* **13**(2021).
14. Bekker, Y.A.C., *et al.* Failure of ketogenic diet therapy in GLUT1 deficiency syndrome. *Eur J Paediatr Neurol* **23**, 404–409 (2019).
15. Kramer, J. & Smith, L. Ketogenic Diet in Glut 1 Deficiency Through the Life Cycle: Pregnancy to Neonate to Preschooler. *Child Neurol Open* **8**, 2329048x211034655 (2021).
16. Nakamura, S., *et al.* Intra-cisterna magna delivery of an AAV vector with the GLUT1 promoter in a pig recapitulates the physiological expression of SLC2A1. *Gene Ther* **28**, 329–338 (2021).
17. Tang, M., *et al.* An early endothelial cell-specific requirement for Glut1 is revealed in Glut1 deficiency syndrome model mice. *JCI Insight* **6**(2021).
18. Nakamura, S., *et al.* Gene therapy for a mouse model of glucose transporter-1 deficiency syndrome. *Mol Genet Metab Rep* **10**, 67–74 (2017).
19. Tang, M., *et al.* Brain microvasculature defects and Glut1 deficiency syndrome averted by early repletion of the glucose transporter-1 protein. *Nat Commun* **8**, 14152 (2017).

20. Pardridge, W.M., Boado, R.J. & Farrell, C.R. Brain-type glucose transporter (GLUT-1) is selectively localized to the blood-brain barrier. Studies with quantitative western blotting and in situ hybridization. *J Biol Chem* **265**, 18035–18040 (1990).
21. Winkler, E.A., *et al.* GLUT1 reductions exacerbate Alzheimer's disease vasculo-neuronal dysfunction and degeneration. *Nat Neurosci* **18**, 521–530 (2015).
22. Yu, S. & Ding, W.G. The 45 kDa form of glucose transporter 1 (GLUT1) is localized in oligodendrocyte and astrocyte but not in microglia in the rat brain. *Brain Res* **797**, 65–72 (1998).
23. Leino, R.L., Gerhart, D.Z., van Bueren, A.M., McCall, A.L. & Drewes, L.R. Ultrastructural localization of GLUT 1 and GLUT 3 glucose transporters in rat brain. *J Neurosci Res* **49**, 617–626 (1997).
24. Morgello, S., Uson, R.R., Schwartz, E.J. & Haber, R.S. The human blood-brain barrier glucose transporter (GLUT1) is a glucose transporter of gray matter astrocytes. *Glia* **14**, 43–54 (1995).
25. Magistretti, P.J. & Allaman, I. Lactate in the brain: from metabolic end-product to signalling molecule. *Nat Rev Neurosci* **19**, 235–249 (2018).
26. Suzuki, A., *et al.* Astrocyte-neuron lactate transport is required for long-term memory formation. *Cell* **144**, 810–823 (2011).
27. Challis, R.C., *et al.* Systemic AAV vectors for widespread and targeted gene delivery in rodents. *Nat Protoc* **14**, 379–414 (2019).
28. Aschauer, D.F., Kreuz, S. & Rumpel, S. Analysis of transduction efficiency, tropism and axonal transport of AAV serotypes 1, 2, 5, 6, 8 and 9 in the mouse brain. *PLoS One* **8**, e76310 (2013).
29. Akman, C.I., *et al.* Topography of brain glucose hypometabolism and epileptic network in glucose transporter 1 deficiency. *Epilepsy Res* **110**, 206–215 (2015).
30. Nonnenmacher, M., *et al.* Rapid evolution of blood-brain-barrier-penetrating AAV capsids by RNA-driven biopanning. *Mol Ther Methods Clin Dev* **20**, 366–378 (2021).
31. Ravindra Kumar, S., *et al.* Multiplexed Cre-dependent selection yields systemic AAVs for targeting distinct brain cell types. *Nat Methods* **17**, 541–550 (2020).
32. Hanlon, K.S., *et al.* Selection of an Efficient AAV Vector for Robust CNS Transgene Expression. *Mol Ther Methods Clin Dev* **15**, 320–332 (2019).
33. Kunze, C., *et al.* Synthetic AAV/CRISPR vectors for blocking HIV-1 expression in persistently infected astrocytes. *Glia* **66**, 413–427 (2018).
34. Dewa, K.I., *et al.* The astrocytic ensemble acts as a multiday trace to stabilize memory. *Nature* **648**, 146–156 (2025).
35. Mendell, J.R., *et al.* Single-Dose Gene-Replacement Therapy for Spinal Muscular Atrophy. *N Engl J Med* **377**, 1713–1722 (2017).
36. Kawabata, H., Konno, A., Matsuzaki, Y. & Hirai, H. A blood-brain barrier-penetrating AAV2 mutant created by a brain microvasculature endothelial cell-targeted AAV2 variant. *Mol Ther Methods Clin Dev* **29**, 81–92 (2023).
37. Chen, X., *et al.* Functional gene delivery to and across brain vasculature of systemic AAVs with endothelial-specific tropism in rodents and broad tropism in primates. *Nat Commun* **14**, 3345 (2023).
38. Nakamura, S., *et al.* Gene therapy for Glut1-deficient mouse using an adeno-associated virus vector with the human intrinsic GLUT1 promoter. *J Gene Med* **20**, e3013 (2018).
39. Graßhoff, H., *et al.* Short regulatory DNA sequences to target brain endothelial cells for gene therapy. *J Cereb Blood Flow Metab* **42**, 104–120 (2022).
40. Vasile, F., Dossi, E. & Rouach, N. Human astrocytes: structure and functions in the healthy brain. *Brain Struct Funct* **222**, 2017–2029 (2017).

41. Matyash, V. & Kettenmann, H. Heterogeneity in astrocyte morphology and physiology. *Brain Res Rev* **63**, 2–10 (2010).
42. Wang, D., *et al.* A mouse model for Glut-1 haploinsufficiency. *Hum Mol Genet* **15**, 1169–1179 (2006).
43. Oddo, M., *et al.* Impact of tight glycemic control on cerebral glucose metabolism after severe brain injury: a microdialysis study. *Crit Care Med* **36**, 3233–3238 (2008).
44. Fray, A.E., Forsyth, R.J., Boutelle, M.G. & Fillenz, M. The mechanisms controlling physiologically stimulated changes in rat brain glucose and lactate: a microdialysis study. *J Physiol* **496**, 49–57 (1996).
45. Dembitskaya, Y., *et al.* Lactate supply overtakes glucose when neural computational and cognitive loads scale up. *Proc Natl Acad Sci U S A* **119**, e2212004119 (2022).
46. Wei, X.Y., *et al.* Neuronal activity-induced GLUT3 plasma translocation supports energy demands for memory acquisition. *Commun Biol* **8**, 1716 (2025).
47. Ashrafi, G., Wu, Z., Farrell, R.J. & Ryan, T.A. GLUT4 Mobilization Supports Energetic Demands of Active Synapses. *Neuron* **93**, 606–615.e603 (2017).
48. Carruthers, A. Facilitated diffusion of glucose. *Physiol Rev* **70**, 1135–1176 (1990).
49. Wichmann, T.O., Damkier, H.H. & Pedersen, M. A Brief Overview of the Cerebrospinal Fluid System and Its Implications for Brain and Spinal Cord Diseases. *Front Hum Neurosci* **15**, 737217 (2021).
50. De Giorgis, V., *et al.* Overall cognitive profiles in patients with GLUT1 Deficiency Syndrome. *Brain Behav* **9**, e01224 (2019).
51. Hao, J., Kelly, D.I., Su, J. & Pascual, J.M. Clinical Aspects of Glucose Transporter Type 1 Deficiency: Information From a Global Registry. *JAMA Neurol* **74**, 727–732 (2017).
52. Goyal, M.S. & Raichle, M.E. Glucose Requirements of the Developing Human Brain. *J Pediatr Gastroenterol Nutr* **66 Suppl 3**, S46–s49 (2018).
53. Sakai, K. & Miyazaki, J. A transgenic mouse line that retains Cre recombinase activity in mature oocytes irrespective of the cre transgene transmission. *Biochem Biophys Res Commun* **237**, 318–324 (1997).
54. Pegg, C.C., He, C., Stroink, A.R., Kattner, K.A. & Wang, C.X. Technique for collection of cerebrospinal fluid from the cisterna magna in rat. *J Neurosci Methods* **187**, 8–12 (2010).
55. Ennaceur, A. & Delacour, J. A new one-trial test for neurobiological studies of memory in rats. 1: Behavioral data. *Behav Brain Res* **31**, 47–59 (1988).
56. Georgiou, E., *et al.* Gene therapy targeting oligodendrocytes provides therapeutic benefit in a leukodystrophy model. *Brain* **140**, 599–616 (2017).
57. Carroll, L., Uehara, H., Zhang, X. & Ambati, B. Tropism of the Novel AAVBR1 Capsid Following Subretinal Delivery. *Int J Mol Sci* **23**(2022).
58. Grieger, J.C., Choi, V.W. & Samulski, R.J. Production and characterization of adeno-associated viral vectors. *Nat Protoc* **1**, 1412–1428 (2006).
59. Guo, P., *et al.* Rapid and simplified purification of recombinant adeno-associated virus. *J Virol Methods* **183**, 139–146 (2012).
60. Zolotukhin, S., *et al.* Recombinant adeno-associated virus purification using novel methods improves infectious titer and yield. *Gene Ther* **6**, 973–985 (1999).
61. Yardeni, T., Eckhaus, M., Morris, H.D., Huizing, M. & Hoogstraten-Miller, S. Retro-orbital injections in mice. *Lab Anim (NY)* **40**, 155–160 (2011).
62. Takahashi, K., *et al.* Induction of pluripotent stem cells from adult human fibroblasts by defined factors. *Cell* **131**, 861–872 (2007).
63. Nishihara, H., *et al.* Advancing human induced pluripotent stem cell-derived blood-brain barrier models for studying immune cell interactions. *FASEB journal : official*

publication of the Federation of American Societies for Experimental Biology **34**, 16693–16715 (2020).

64. Nishihara, H.*, et al.* Differentiation of human pluripotent stem cells to brain microvascular endothelial cell-like cells suitable to study immune cell interactions. *STAR Protocols* **2**(2021).

65. Matsuo, K., Engelhardt, B. & Nishihara, H. Differentiation of Human Induced Pluripotent Stem Cells to Brain Microvascular Endothelial Cell-Like Cells with a Mature Immune Phenotype. *Journal of Visualized Experiments* (2023).

66. Matsuo, K.*, et al.* Establishment of a novel amyotrophic lateral sclerosis patient (TARDBPN345K/+)-derived brain microvascular endothelial cell model reveals defective Wnt/β-catenin signaling: investigating diffusion barrier dysfunction and immune cell interaction. *Frontiers in Cell and Developmental Biology* **12**(2024).